Event generation for beam dump experiments

Buonocore, Luca ; Frugiuele, Claudia ; Maltoni, Fabio ; Mattelaer, Olivier ; Tramontano, Francesco

Abstract: A wealth of new physics models which are motivated by questions such as the nature of dark matter, the origin of the neutrino masses and the baryon asymmetry in the universe, predict the existence of hidden sectors featuring new particles. Among the possibilities are heavy neutral leptons, vectors and scalars, that feebly interact with the Standard Model (SM) sector and are typically light and long lived. Such new states could be produced in high-intensity facilities, the so-called beam dump experiments, either directly in the hard interaction or as a decay product of heavier mesons. They could then decay back to the SM or to hidden sector particles, giving rise to peculiar decay or interaction signatures in a far-placed detector. Simulating such kind of events presents a challenge, as not only short-distance new physics (hard production, hadron decays, and interaction with the detector) and usual SM phenomena need to be described but also the geometry of the detector has to be taken into account for a reliable estimate of the event yield and distributions. In this work, we describe a new plugin to the MadGraph5$_a$$MC@NLOplatform, whichallowsthecompletesimulationofnewphysicsprocessesrelevantforbeamdumpex$

DOI: https://doi.org/10.1007/jhep05(2019)028

Published for SISSA by Springer
Received: January 3, 2019
Revised: March 28, 2019
Accepted: April 22, 2019
Published: May 6, 2019

Event generation for beam dump experiments

Luca Buonocore,[a,b] **Claudia Frugiuele,**[c] **Fabio Maltoni,**[d,e] **Olivier Mattelaer**[d] **and Francesco Tramontano**[b]

[a] *Physik Institut, Universität Zürich, Winterthurerstr. 190, 8057 Zürich, Switzerland*
[b] *Dipartimento di Fisica, Università di Napoli Federico II and INFN, Sezione di Napoli, via Cintia, 80126 Napoli, Italy*
[c] *Department of Particle Physics and Astrophysics, Weizmann Institute of Science, Rehovot 7610001, Israel*
[d] *Centre for Cosmology, Particle Physics and Phenomenology (CP3), Université catholique de Louvain, B-1348 Louvain-la-Neuve, Belgium*
[e] *Dipartimento di Fisica e Astronomia, Università di Bologna and INFN, Sezione di Bologna, via Irnerio 46, 40126 Bologna, Italy*

E-mail: lbuono@na.infn.it, claudia.frugiuele@cern.ch, fabio.maltoni@uclouvain.be, olivier.mattelaer@uclouvain.be, francesco.tramontano@na.infn.it

Abstract: A wealth of new physics models which are motivated by questions such as the nature of dark matter, the origin of the neutrino masses and the baryon asymmetry in the universe, predict the existence of hidden sectors featuring new particles. Among the possibilities are heavy neutral leptons, vectors and scalars, that feebly interact with the Standard Model (SM) sector and are typically light and long lived. Such new states could be produced in high-intensity facilities, the so-called beam dump experiments, either directly in the hard interaction or as a decay product of heavier mesons. They could then decay back to the SM or to hidden sector particles, giving rise to peculiar decay or interaction signatures in a far-placed detector. Simulating such kind of events presents a challenge, as not only short-distance new physics (hard production, hadron decays, and interaction with the detector) and usual SM phenomena need to be described but also the geometry of the detector has to be taken into account for a reliable estimate of the event yield and distributions. In this work, we describe a new plugin to the MadGraph5_aMC@NLO platform, which allows the complete simulation of new physics processes relevant for beam dump experiments, including the various mechanisms for the production of hidden particles, namely their decays or scattering off SM particles, as well as their far detection, keeping into account spatial correlations and the geometry of the experiment.

Keywords: Beyond Standard Model, Chiral Lagrangians, Perturbative QCD

ArXiv ePrint: 1812.06771

https://doi.org/10.1007/JHEP05(2019)028

JHEP05(2019)028

Contents

JHEP05(2019)028

1 Introduction

Experiments at the LHC have yet not reported any sign of physics Beyond the Standard Model (BSM). Nevertheless, the problem of reconciling our description of the fundamental interactions and particles with long-standing problems, such as the matter-antimatter asymmetry in the Universe, the evidence for dark matter from many astrophysical and cosmological observations and the origin of the neutrino masses, becomes ever more pressing. Many ideas have been proposed, some of which addressing one problem at the time,

others, more ambitious, providing solutions to two or more open questions at the same time. In this context, a recurrent theme is the hypothesis that a hidden sector involving new light particles, might be coupled to the Standard Model via, for instance, one of the three portals (scalar, fermion and vector) in a feeble way. Such scenarios can provide not only dark matter candidates, but also other states, such as heavy neutral leptons, vectors, scalars, which could be long-lived and also possibly decay back to SM particles.

To prove the existence and measure the properties of such elusive particles is extremely difficult. The situation is in fact similar to neutrino production and detection:[1] as the energy does not pose a hindrance, one is lead to consider high-intensity facilities and design experimental setups that maximise the rates. In short, one needs very intense beams and then let such beams cross a heavy and instrumented target to detect their scattering or, if necessary, to create a decay tunnel as long as possible to observe their decay products. A first example is NA62 [3, 4] which can run in a beam dump mode and is expected to collect data in this configuration soon. The DUNE [5] experiment will be operational in 2026 to study neutrino oscillations. As a by-product it could also search for hidden sector particles. The SHiP experiment [6, 7] has been designed on purpose to search for such light and feebly interacting particles originated in interactions of 400 GeV/c protons produced by the CERN SPS [8]. More recently, other proposals have been put forward to also exploit proton collisions at the LHC experiments with detectors placed not very far from the collision points, namely, the CODEX-b [9], MATHUSLA [10, 11], FASER [12, 13] and AL3X [14] experiments.

In the present paper we address the issue of how to efficiently simulate the production of a flux of particles belonging to the hidden sector and their subsequent interactions and/or decays. In the following, we will generically call a Beam Dump Facility (BDF) every experiment where a known flux of primary SM probes strikes on a fixed target and a detector is placed in an optimal position with respect to the target, with the aim of detecting either neutrinos or a new kind of feebly interacting particles produced off the primary beam interaction. The case of a detector placed close to a collider experiment such as those proposed in [9–13] can be equally treated within our framework without any modifications. In practice, sensitivity studies of such experiments to new physics phenomena, rely on the simulation of two distinct processes, one where the new particles are produced and the other where the new particles (or their decay products) interact with a detector placed at some macroscopic distance, from tens of meters to thousands of kilometers.

The production of a feebly interacting particle in a beam dump can proceed through at least three phenomenologically different phenomena: i) its prompt production in the high energy scattering of the primary beam particle with a nucleus in the target; ii) as the result of the decay of SM particles produced in the primary collision or in the cascade process in the target; iii) through the bremsstrahlung process of primary or secondary particles in the target. The detection, on the other hand, will proceed either through the decay in flight of new particle back to visible SM final states or directly through the scattering with the matter in the detector.

[1] In this case, it is somewhat instructive to remind that even though we know a lot about neutrinos properties by now, τ neutrinos are still quite unknown; with nine charged current τ neutrino events identified by the DONUT experiment [1] and 10 by the OPERA experiment [2] it is by far the least known of the SM particles.

JHEP05(2019)028

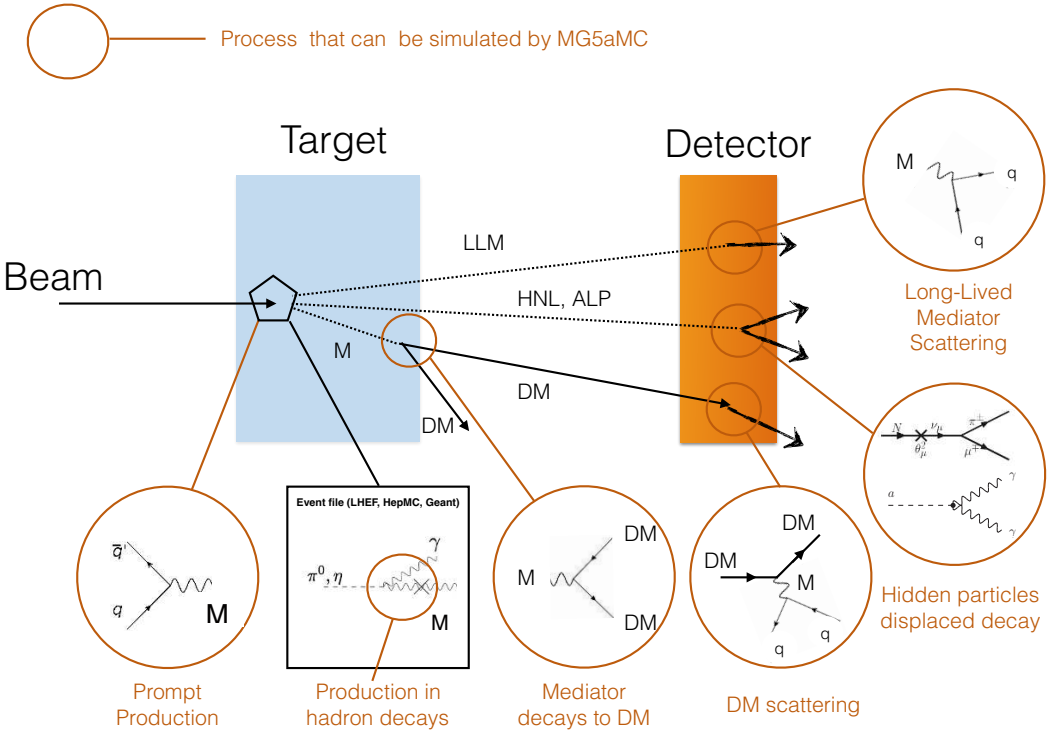

Figure 1. Schematic view of relevant processes that might happen at a BDF and can be computed/simulated within MG5aMC.

The aim of this paper is to provide an implementation that allows the simulation of the complete chain of subprocesses, from the production to the final detection at a BDF in one go. Our starting point are FeynRules [15–17] for the implementation of the new physics model lagrangian and MadGraph5_aMC@NLO [18, 19], MG5aMC for short, for providing the necessary short-distance physics elements, the automatic production of particle-level unweighted events and the framework. To achieve maximal flexibility we provide the implementation as a MG5aMC plugin, in line with other recently developed applications [20–22]. Figure 1 shows a sketch of the elements of the simulation which are automatically combined in our implementation. These functionalities are available so that samples of unweighted events in a standard format can be generated in a single step and eventually passed to the simulation of the detector response. For the rest of the paper we dub the MG5aMC plugin for the simulation of hidden particle effects at beam dump facilities with the short-hand name MadDump.

An important aspect of our implementation is that it provides the elements of the simulation that are related to BSM physics in a single framework. This entails a number of advantages. First, it eliminates the possibility of making mistakes in the generation or in the combination of event samples for the production and the detection stages. This is particularly relevant when scanning over the parameters of a BSM model, where, although every step is simple in principle, the combinatorics and the bookkeeping would make the whole construction cumbersome. Second, by using functionalities already present

JHEP05(2019)028

in MG5aMC it allows to fully automate the scanning over the BSM parameters. Third, once implemented in FeynRules and available in the UFO format, the same BSM model and parameter points can be constrained in different contexts within the same framework, for instance, in collider physics using MadAnalysis5 [23–25] recasting capabilities or in MadDM [22, 26, 27].

In MadDump the primary flux of Standard Model probes that can generate the hidden particles has to be provided by the user. As shown in figure 1, it can be either the original beam hitting the target, or the flux of hadrons following the hard interaction that can produce the hidden particle through their decays. In the former case, the user has just to provide the specific particle code of the probe and its energy in the laboratory frame, while for the latter case the flux can be given as an event file featuring the decaying particle momenta and specifying the particle identifier. Note that, for the case of hidden particles generated in the target from meson decays, our approach is more flexible than just directly linking event generators like Pythia8 [28, 29] or HERWIG7 [30] as it allows, in principle, to later include other effects, such as the cascade production of secondary particles which in some cases could be relevant. MadDump is able to handle event files in all formats of the most used event generators like LHE or HEPMC. Another important ingredient is the geometry of the BDF, which is provided by the user in a dedicated file.

The paper is organised as follows: in section 2 we introduce the algorithms at the core of MadDump. In section 3 we present illustrative examples of possible applications, considering physics cases relevant for the SHiP experiment. Conclusions and the perspectives of the present work are given in section 4. In three appendices A, B and C we provide many details on the numerical techniques employed and the associated uncertainties, while appendix D documents the scripts that produce the results presented in section 3.

2 Approach

The first important aspect of our implementation is the idea of considering the beam dump experiment as a two-step process:

- *Production*: hidden particle flux generation upon interaction of the beam with the target;
- *Detection*: interaction of the hidden particles (or their decay products) in the (possibly far-placed) detector.

While both steps depend on the details of the new physics model and therefore they have to be considered together, it is possible to factorise the simulation into two independent steps: the results of the *Production* phase simulation are used to build a (two-dimensional) parametrisation of the incoming hidden particle flux hitting the detector and leading to different signatures in the detector. By disentangling the *Production* from the *Detection* phase and the corresponding event generation into two subsequent steps, the possibility of following the full history, from production to the final signature in the detector, of each event is lost. However, the gain in efficiency in the event generation is enormous, an element which is a key aspect in the simulation of a high-intensity experiment.

JHEP05(2019)028

The second important aspect of MadDump is that it has been designed as a plugin of MG5aMC. In other words, it heavily relies on already existing modules which are at the core of MG5aMC, such as the phase space integration provided by MadEvent and the decay package MadSpin [21], integrating them with functionalities that are specifically required for BDF's, so the various steps of the simulation can be undertaken to obtain the final result in one go. Among the key new functionalities, we stress

- the determination of doubly differential scatter data in the *Production* phase of non-standard particle beams and their support in the *Detection* phase;
- the support of HepMC as input format with the aim of making easier the interplay with other Monte Carlo generators like Pythia8 or HERWIG7.

The third aspect is the underlying idea of factorising SM physics from the BSM one, whenever possible. The former, while accessible via standard MC tools, is in general quite involved and needs the modeling of many effects. Being strongly dependent on the particular experimental setup, a dedicated simulation of the target and/or detector effects is almost always needed. However, while cumbersome, this part of the simulation does not have any dependence on the new physics model considered and can be taken care once for all. On the other hand, the new physics short-distance part by definition depends on the details of the model and therefore has to be generated/considered for each different data interpretation. Fortunately, it can be described quite easily from first principles and dealt with by usual or especially developed MG5aMC modules.

2.1 Production

In a typical beam dump experiment, a collimated and mono-energetic beam of protons or electrons impinges on a thick target, at rest in the laboratory frame. A copious number of SM particles is generated both in primary and subsequent secondary interactions inside the target, which is designed to maximise the particles yields. The production of hidden sector particles may proceed according to different mechanisms. In the following, we focus on two cases, i.e.,

- prompt production in primary or secondary beam interactions
- rare meson decays.

Without loss of generality, we consider the case of proton beam dump experiment, keeping in mind that other situations can be dealt with by MadDump in a completely analogous way.

Depending on the specific BSM physical case (model and parameter point of interest), the prompt production may be described in perturbation theory and it can be treated directly in MadDump. In this case, the main input is the BSM Lagrangian (in the UFO format) which fixes the hidden sector model and its interactions with the SM particles. For example, in a model where a new massive vector mediator couples to quarks and Dark Matter (DM) fermionic particles, the main production mechanism resembles Drell-Yan production and decay at fixed target experiments. This description must, however,

JHEP05(2019)028

be consistent with the typical scales characterising the model. For instance, in the above example the mass of the mediator must be larger than the QCD scale for the computation to be reliable.

As stated above, the main goal of MadDump is to handle BSM interactions and then embed them consistently into a complete and modular simulation chain which can take into account the rest of the SM interactions, possibly also using other inputs. In particular, an accurate simulation of the cascade production of hadronic particles, mesons and baryons, is expected to be handled by other MC tools or dedicated simulations, which can fully include parton showers, hadronisation, nuclear effects, meson decays and so on. This part can be very important if hidden particles are produced in the decays of mesons. In that case, the meson production is assumed to be simulated independently. MadDump, on the other hand, by parsing the event files[2] describing the beam-target event takes care of the decay of mesons into hidden particles, employing for example, an effective field theory approach, which can also be implemented at the level of the UFO. In this way, mesons are considered on the same footing of the elementary particles in the model and their decays occur through interaction vertices that can be handled by MG5aMC in the usual way. Examples of both prompt production and meson decay studies are given in section 3.

Either way, by the hard-interaction or via the decay of mesons, hidden particles are created, which fly out of the target close to the forward direction. The hidden particles produced during the beam dump, however, do not form a standard collimated and mono-energetic particle beam. On the contrary, they have a spatial distribution, they are produced in different points inside the volume of the target, and a phase space, i.e., a non trivial four-momenta spread, distribution. Assuming that the hidden particles travel freely until they eventually enter in the active region of the detector, after macroscopic distances that can go from meters to hundreds or thousands of kilometers, we can describe the beam of hidden particles by means of a multi-differential flux function

$$\phi_\chi(E, \vec{x}) = \frac{dn_{\rm DM}}{dE d\vec{x}}, \tag{2.1}$$

where the vector $\vec{x}$ denotes the collection of all the other relevant kinematical variables (angles, spatial distribution of the hidden particles production point within target, etc.), but the energy. The flux function in general not known a priori and/or in an analytical form since it represents the result of scattering/decay processes in the *Production* phase. This distribution is implicitly determined by the simulation of the *Production* phase and in turn it can be extracted from a sufficiently large sample of production events. In practice, since the flux depends on the particular BSM model and the specific production mechanism, it cannot be fit it once and for all (as for the proton pdf). An on-the-fly fitting procedure is needed that is fast, robust and flexible.

[2]We remark the importance of having an easy way to interface MadDump with other generators. Indeed, as we argued for the case of meson decay, MadDump can take as input the results of other tools in the form of event files. This is the main reason why the HepMC format [31] for the input files was chosen as an option for MadDump.

JHEP05(2019)028

2.2 Detection

The final detection of the hidden particles might occur according to the two distinct physical processes

- the hidden particle interacts with the active volume of the detector, resulting in a neutrino-like signature;
- the hidden particle decays to SM particles inside a dedicated decay tunnel (included of what we dub "detector"), resulting in a "displaced vertex" signature.

The interaction of the hidden particle with the detector turns out to be the most difficult part to simulate. One can exploit some approximations and different Monte Carlo techniques to obtain a generator with a satisfactory level of accuracy. On the contrary, as we will discuss later, in the displaced decay case, the same complications do not arise and the situation is much easier to handle. Let us discuss first the interaction case.

2.2.1 Interactions of hidden particles in the detector

The outcoming flux of hidden particles from the *Production* phase, eq. (2.1), corresponds to the incoming hidden particles flux of the *Detection* phase. Our strategy is to parametrise the flux by using *Production* event samples and use it as a generalised partonic distribution function (pdf) for the needed computations in the *Detection* phase. In doing so, we will also able to parametrise not only the acceptance of the detector but also some of the efficiencies/features that are model dependent.

The total interaction cross section with the fiducial volume of the detector is obtained by convoluting of the flux function $\phi_\chi(E, \vec{x})$ with the elementary cross section $\hat{\sigma}_I$ for the "partonic" sub-process

$$\mathrm{HP} + X \to \mathrm{HP} + X', \tag{2.2}$$

where X represents the SM matter particle in the detector and "HP" the hidden particle. Our implementation is able to handle:

- elastic electron scattering, $X = e^-$
- deep inelastic scattering of nucleons (DIS), $X = u, d, s, c$.

The geometrical detector acceptance sets the integration limits in the convolution integral. This is equivalent to introduce a weight function $W(E, \vec{x})$ which is 0 if the point does not pass the acceptance cut and 1 otherwise. In this way, it is possible to restore the integration limits to their full ranges. This simple idea is the basis of more sophisticated re-weighting strategies in Monte Carlo integration. We can exploit these techniques with the aim of modeling in a realistic way the detector efficiency. For example, due to its shape and composition, the particles entering the detector may travel a longer or shorter path inside its volume. Correspondingly, the probability that the particles interact inside the detector will be greater or lesser resulting in an efficiency function depending on kinematical variables of the incoming particles. We can effectively describe this effect giving a suitable weight $W(E, \vec{x})$ to each incoming hidden particle penalising those which will travel a shorter

JHEP05(2019)028

path. To this aim, we have introduced in our framework the possibility of introducing a re-weighting procedure and we have extensively tested/used it to describe some common detector effects. The user can easily customise the weight function in order to refine the simulation at will.

Our master formula for the *Detection* cross section σ_D is given by:

$$\sigma_D = \int dE \int d^n x \, \phi_\chi(E, \vec{x}) \, W(E, \vec{x}) \, \hat{\sigma}_D(E). \tag{2.3}$$

The crucial point here is that the partonic cross section $\hat{\sigma}_D$ does not depend on the other variables but the energy, as it follows directly from the Lorentz invariance of the interaction among point-like particles. Due to this property we are allowed to formally perform the integral over the $\vec{x}$ vector before performing the convolution with the partonic cross section leading to the introduction of an effective one-dimensional energy pdf:

$$\tilde{\phi_\chi}(E) = \int d\vec{x} \phi_\chi(E, \vec{x}) W(E, \vec{x}) \implies \sigma_D = \int dE \tilde{\phi_\chi}(E) \hat{\sigma}_D(E). \tag{2.4}$$

Before proceeding further, we discuss some practical implications of the above formula. The 1D-function $\tilde{\phi_\chi}(E)$ can be obtained through a simple 1D fit of the energy histogram of the input DM production events, after having re-weighted them by the weight function $W(E, \vec{x})$. According to eq. (2.4), this is the only ingredient needed to compute the total cross section, which in turn is crucial to extract the hidden particles yields in the detector. Up to this point, the simulation of a collimated (along the beam axis) but not mono-energetic beam of hidden particles particle impinging on the detector is achieved. However, this is not sufficient to develop a full event generator of unweighted "interaction events". A complete event reconstruction that gives access to correlations (between energies, positions, angles), may be of great importance. It can allow to study possible kinematical cuts with the aim of maximising the signal yield with respect to the backgrounds, and to accurately model detector effects. For example, due to different energy-angular correlations of the DM particles with respect to the neutrino ones, it is possible to have a signal-enriched sample of events for off-axis detector configurations, as pointed out in ref. [32]. Hence, in principle this information might be useful to design optimised experimental configurations. Moreover, the output events can be further post-processed exploiting for example parton shower programs or other dedicated tools in order to have a better estimates of the detector efficiency.

In principle, given the "trivial" dependence of the partonic cross section on the parameters $\vec{x}$, we can assign them a posteriori on a event-by-event base according to the distribution

$$P(\vec{x}) d\vec{x} = \phi_\chi(\overline{E}, \vec{x}) W(\overline{E}, \vec{x}) d\vec{x} \,, \tag{2.5}$$

at fixed $E = \overline{E}$, where $\overline{E}$ is the energy of the current event. In practice, the procedure underlying the above formula is limited by the computational issue of performing a robust and reliable multi-dimensional fit, since the incoming particle flux is not known analytically. As mentioned above, our fitting procedure relies on the point-like approximation of the target in the primary interaction. In a typical beam dump experiment, the distance between the production target and the near detector is greater than the characteristic size of the

JHEP05(2019)028

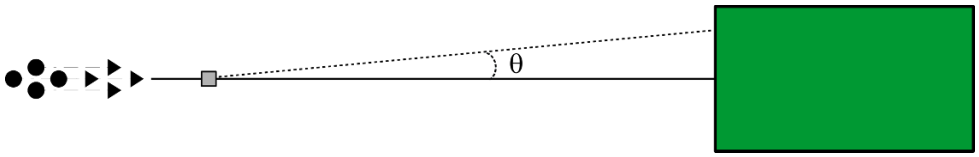

Figure 2. Production and detection of dark matter at a beam-dump experiment: a sketch of the setup and the kinematics.

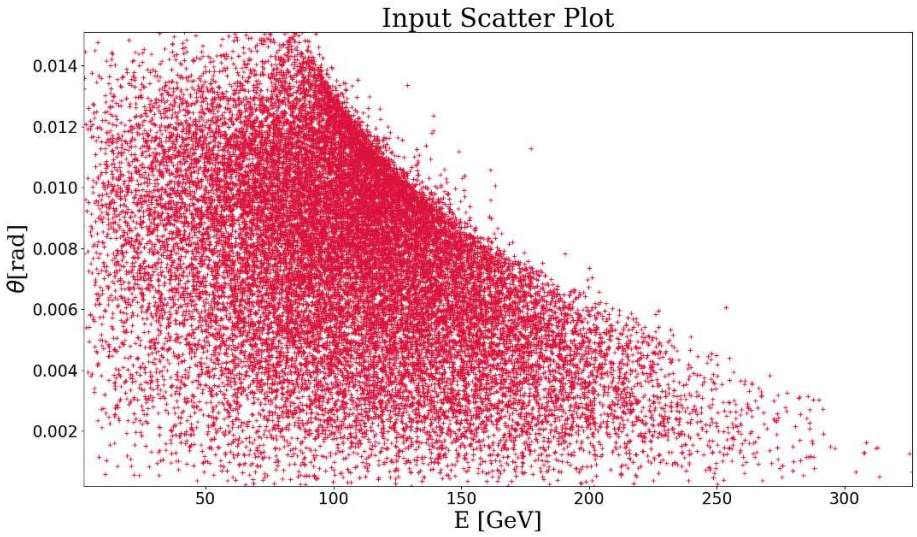

Figure 3. Input 2D-Scatter plot in the DM $E-\theta$ plan. As example, we consider DM particles produced by a Dark Photon-like mediator, which enter a SHiP-like detector.

target, so that the point-like target approximation is a reasonable first approximation. Under this assumption, the complexity of the problem reduces considerably. As depicted in figure 2, just three kinematical variables are needed to describe the incoming flux impinging the detector: the energy E, the polar angle θ and the azimuthal angle ϕ around the beam axis. Furthermore, the physics occurring at the production point is invariant under a rotation around the beam axis resulting in flat distributions for the azimuthal correlations. Hence, the only relevant correlations are the $E-\theta$ ones. In figure 3 we show a typical plot of the production scatter data, which enter into the neutrino detector, in the $E-\theta$ plane for a SHiP-like configuration [6, 7].

In order to generate E, θ values distributed in the same way, we have developed a numerical 2D-fitting algorithm which is fast, robust and automated. The main design concepts are based on the adaptive algorithms exploited in Monte Carlo integrators like VEGAS [33] and FOAM [34]. Our algorithm produces a 2D-mesh of bins for the 2D-histogram of the input points in the (E, θ)-plane in such a way that the histogram heights are flat. It is based on a deterministic procedure: we apply a sequence of alternate splittings, one along the x-axis and one along the y-axis, according to a democratic principle of equal weights. Further details on this technique can be found in appendix A. As an example, in figure 4, we show the 2D-mesh associated to the scatter data in figure 3.

JHEP05(2019)028

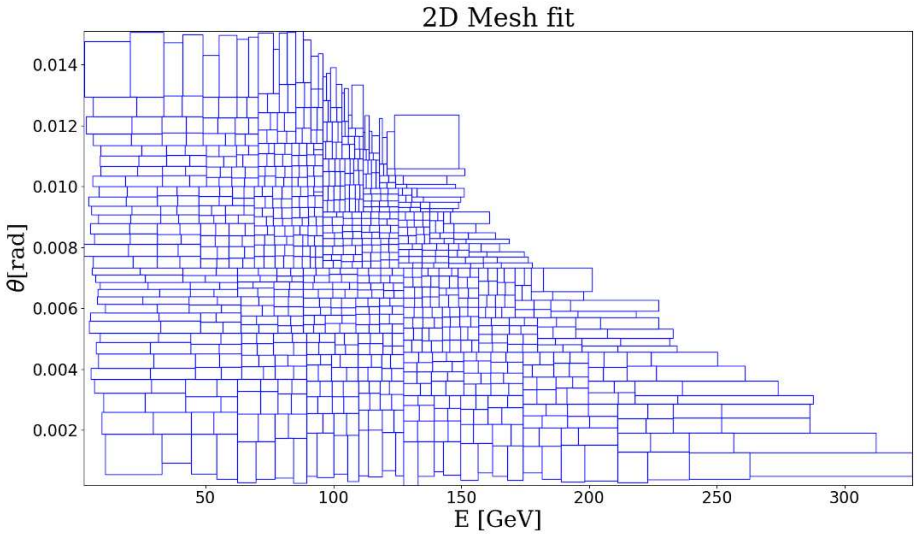

Figure 4. Result of the fitting procedure. The area of the cells in the mesh is proportional to the number of events in the cells.

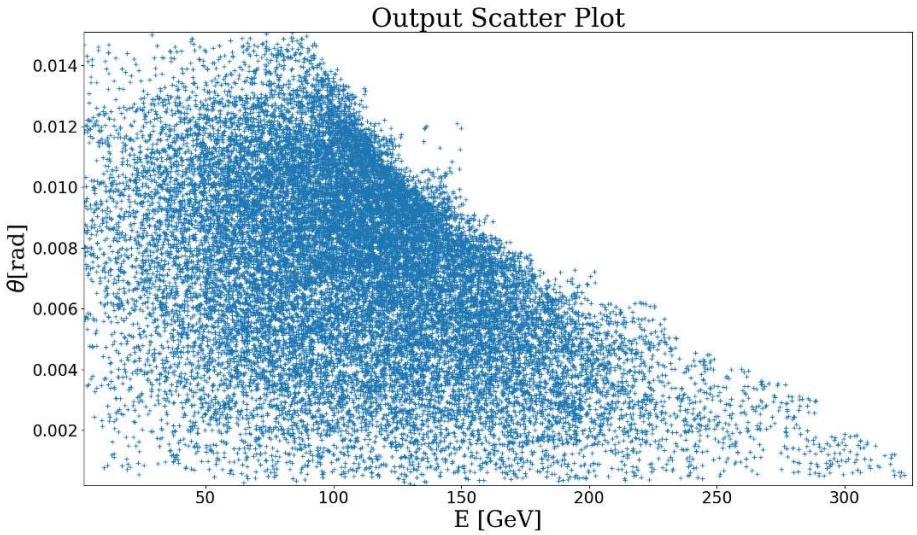

Figure 5. Re-generated 2D-scatter plot starting from the fitted 2D-mesh. See figure 3 for the comparison with the original plot.

Starting from this mesh, we can generate new E, θ points with the same distribution as the original ones. The result is plotted in figure 5, where the goodness of the procedure can be appreciated. The inspection of these plots does not replace quantitative estimators as the one defined in the appendix B, but it can serve for a quick survey on the internal machinery and as a sanity check. The flag `testplot` in the `fit2D_card.dat` turns on the print out the content of these plots in a table format. We pass now to describe the generation of the azimuthal angle ϕ. As already stated above, at fixed θ, the ϕ distribution of the flux is flat due to the symmetry with respect to the beam axis at the production point. The only kind of angular correlations which can be introduced are of geometrical nature

JHEP05(2019)028

and depend on the shape of the detector. In the case of an off-axis detector, or even simply of a detector on-axis with a rectangular surface exposed to the flux of a hidden particle, the allowed angular region does not coincide with the full angular range $[\theta_{\min}, \theta_{\max}] \times [0, 2\pi]_\phi$. Since the distributions are flat in the azimuth ϕ, it is convenient to parametrize the surface of the detector in terms of a single interval with constant endpoints in θ and θ-dependent regions for the variable ϕ. Geometrically, this means that we first fix a value of θ and consider the circular projection, which is obtained by varying ϕ in the range $[0, 2\pi]$, onto the transverse plane at the distance where the surface of the detector lies. Then, we determine the ϕ regions for which the circumference is inside the surface of the detector. For example, let us consider the case of an on-axis detector with a rectangular shape, as in the SHiP experiment. For small values of θ, the circular projection will lie entirely inside the rectangular surface so that all values of ϕ in $[0, 2\pi]$ are accessible. On the other hand, when we pick a θ value big enough, we get the situation in which the circular projection intersects the rectangle in four (or even eight points). In this case, the allowed values of ϕ lie in two (four) distinct intervals, which are completely determined by the given value of θ. The choice of the above parametrization allows us to handle in a simple fashion the unweighted generation within the geometrical acceptance only. As first step, we follow the procedure outlined above to generate a θ angle. Then, we pick with uniform probability one of the available regions for the azimuth and, finally, we generate a ϕ value inside that region, again according to the uniform distribution. In figure 6, we compare the angular correlations as obtained by the original scatter points which cross the detector surface and the ones we reconstructed following our strategy. Again, the agreement is fairly good. We stress that the above procedure is fully consistent with the re-weighting strategy outlined at the beginning, which we summarise here:

1. we first build the one-dimensional energy pdf on top of the original (unweighted) scatter points re-weighted by the effective function W, which takes into account, for example, that for some θ values, there are ϕ values not allowed;

2. we then reconstruct the missing variables in their actual ranges.

We exploited the same re-weighting strategy to modeled the full 3D-geometry of the detector. Indeed, up to this point, the same weight has been assigned to each particle direction. More technical details on this procedure are reported in appendix C. Depending on the specific new physics model, the interaction between hidden particles and the SM matter in the detector can be based on different types of processes:

- elastic scattering off electron;

- DIS-like scattering off nuclei;

- elastic and coherent scattering off nuclei.

In principle, the processes included in the above list can be easily simulated in our framework if a suitable model file is supplied, at least for the first two cases.

JHEP05(2019)028

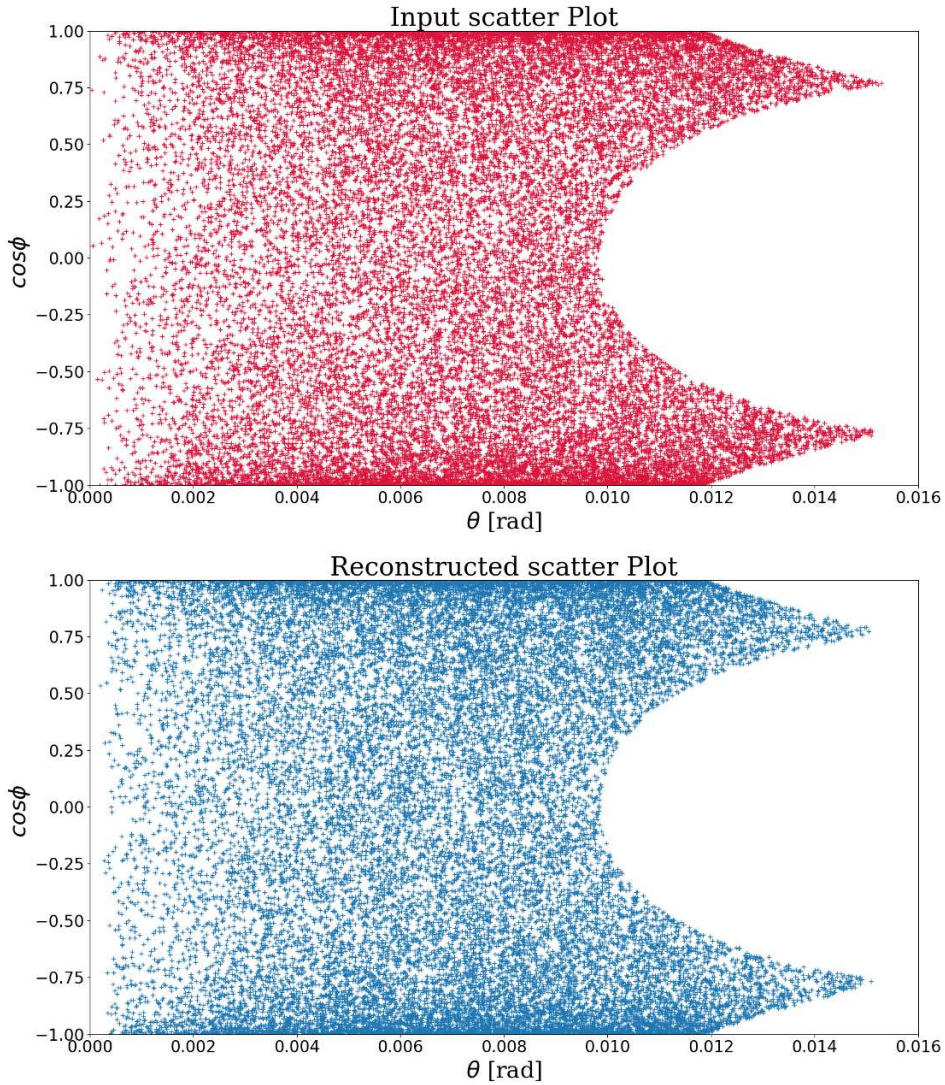

Figure 6. Comparison plot between the $\theta - \phi$ correlation as given by the original input scatter data (top panel) and by the re-generated points (bottom panel) obtained according to the procedure outlined in the main text.

2.2.2 Displaced decays

In the case of displaced decays, the algorithm simplifies considerably. The decay process does not require the regeneration of the events and then the issue of their full reconstruction does not arise. Indeed, the decay can be generated event-by-event on top of the incoming flux of the unweighted events. The probability that a given particle decays in a specified decay channel i after having traveled a distance l from the production point is given by

$$P_i(l) = \mathrm{Br}_i \times (1 - e^{-l/\lambda}), \qquad \lambda = \frac{\gamma\beta}{\Gamma} \tag{2.6}$$

where Br_i is the branching ratio for the i-channel, γ and β are, respectively, the Lorentz factor and the velocity in the laboratory frame of the decaying particle, and Γ is its width.

JHEP05(2019)028

The displacement from the production to the decay point can be determined starting from the partial decay widths. The latter, for the given BSM model, are computed on-the-fly according to the actual parameters of the simulation (the so-called "auto-width" option [35]). This feature in combination with the "auto-scan" mode [36], both provided by MG5AMC, allows for a complete simulation scan over the relevant parameter space. In the present version of MadDump, the displaced decay events are not forced to be generated inside the actual decay vessel. It is only as the last step of the simulation, that a rejection of the events that occur outside the detection volume happens. The algorithm could be improved by reweighting each event according to the distance that the decaying particle could actually travel inside the decay vessel.

2.3 Details of the implementation

In the procedure outlined above, we encoded all the details of the detector in the efficiency function W, eq. (2.3). It acts as a weight function for each incoming dark matter particle event. Despite the general ground of the method, its actual implementation leads unavoidably to some design choices, in particular regarding the user interface. Here, we will present our design philosophy and we will give the main details of the implementation.

We followed a pragmatic approach. Indeed, while the full knowledge of the efficiency function W is not available a priori (of course, it depends on the specific situation under consideration), on the other hand, some basic aspects of the geometry of the detector can be taken into account in a general manner. Our idea has been that of providing a collection of standard detector shapes and configurations which can approximate the geometry of a realistic experiment. The main settings can be found in the `fit2D_card.dat` card file. Some of them are shared by all of the possible configurations: the distance from the target to the detector, the average density of detector, the Z/A ratio (which is important to determine the correct number of electrons in the fiducial volume of the detector). They are set by the following commands

```
set d_target_detector value
set detector_density value
set Z_average value
set A_average value
```

where *value* stands for the desired numerical value. For what concerns the units, it is understood that all the lengths are in cm and all weights in g. Going to more specific cases, we include the possibility to handle both on-axis (default choice) and off-axis configurations. In the former case, we consider two possible shapes of the detector:

- parallelepiped with the axis parallel to the beam axis (default choice),
- cylinder with the axis parallel to the beam axis.

JHEP05(2019)028

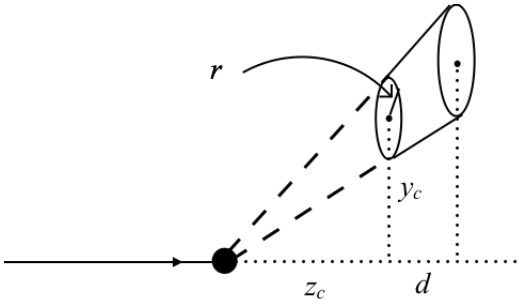

Figure 7. Schematic view of the off-axis configuration implemented in MadDump.

They can be set by the following commands

1. ```
   set parallelepiped True
   set x_side value
   set y_side value
   set depth value
   ```

   In the above, `x_side`, `y_side` are the dimensions in the transverse plane, while `depth` is the dimension along the beam axis.

2. ```
   set parallelepiped False
   set cylinder True
   set theta_max value
   ```

   Here, `theta_max` is the angular aperture (in radians), using as pivot the production point, from the beam axis to the edge of first circular surface of the cylinder. In other words, the radius of the cylinder is given by the formula

$$r = \texttt{d\_target\_detector} \times \tan \texttt{theta\_max}. \tag{2.7}$$

For the off-axis mode, a beta version is available in the current release of the plugin. We have implemented for the moment only the simplest geometry given by a truncated cone with circular basis and with the lateral surface radial with respect to the production point, as illustrated in figure 7. The list of commands to enable this mode is as following

```
set off_axis true
set yc value
set radius value
set depth value
```

In this case, using as reference figure 7, `d_target_detector` sets the distance between the production point and the detector surface projected onto the beam axis (z_c), `yc` is the distance of the center of the first circular surface from the beam axis, `radius` (r) is its radius and `depth` (d) is the distance among the two circular surfaces of the detector projected along the beam axis.

JHEP05(2019)028

In this way, we provide the user with some basic control over the geometry of the detector. In the language of the efficiency function W, we handled only the regions in which W vanishes (sharp edges) while we still have uniform weights inside the geometrical acceptance, i.e we are modeling the geometry but we are still considering an ideal detector with efficiency equals to one. Different shapes of the detector can easily be handled by considering their embedding into one of the available shapes and rejecting a posteriori the events that fall outside the actual fiducial volume. For time being, we refrain ourselves to add further options in the spirit to keep the interface as simple as possible. The full specification of the efficiency function is possible by acting at the level of the plugin source code. In the simple case the customize W function does not affect the available geometries, the modification of the source code is restrict to code W in the function `eff_function` which is part of the python module `meshfitter2D.py`. In the general case, it is required a deeper knowledge of the source code. Further technical details on this point, which are beyond the general strategy discussed in the present paper, will be part of the documentation of the plugin.

Before concluding, some remarks are needed. From our point of view, the strategy outlined in the above should be of main interest for the phenomenologist and for the model builder to have an effective and fast tool for their studies, which captures the main aspects of the experiment under consideration. The most realistic simulation of the detector effects is far beyond the scope of our plugin and it represents, in general, the result of the great efforts of a whole experimental collaboration. In this context, we think that our tool is still useful and appealing as it stands as a Monte Carlo events generator which can be easily instructed to deal with new models. We stress that having access to the scattering events makes it possible the interplay with dedicated tools (as Geant4) for the full reconstruction of the visible track inside the detector.

3 Illustrative examples

In this section we provide some illustrative applications of MadDump, considering three new physics models and making the corresponding predictions for the SHiP experimental setup [7]. We stress that the SHiP facility configuration used in the following is based on the one developed for the Technical Proposal in 2015 [7]. Since then, the SHiP Collaboration has continuously improved its setup aiming at higher sensitivity in the different channels. The newest setup as well as the corresponding background estimates are not yet available. The analyses reported in this paper will have to be redone once the updated information becomes available. Table 1 summaries the relevant input parameters which specify also the geometry of the apparatus. In particular, we determine the number of detectable events for each model in a typical run and then using the expected rates for the background processes reported in [7] we estimate the experimental sensitivities at 99.73% confidence level, which corresponds to the 3σ contour, and compare them with existing limits. Previous estimate of SHiP sensitivity has been provided in [37] where a publicly available tool BdNMC to simulate dark matter production and scattering at proton fixed target experiments was also presented.

JHEP05(2019)028

parameter	value
# proton-on-target	$2 \cdot 10^{20}$
detector configuration	on-axis
distance target-detector	5650 cm
detector density	$3.72\,\mathrm{g/cm^3}$
detector shape	parallelepiped x-side: 187 cm y-side: 69 cm z-side: 200 cm
detector efficiency	1

Table 1. Main input values used for the simulation of the SHiP detector geometry, as reported in ref. [7].

3.1 Quark-DM scattering: leptophobic portals

Let us first consider the case where an hidden particle that could be a dark matter candidate interacts with the visible sector via a new leptophobic force. This is a good benchmark model to study quark-DM scattering, in particular we will focus on signatures of deep inelastic scattering.

3.1.1 Vector portal: baryonic U(1)$_B$

The simplest possibility for a leptophobic force mediated by a spin 1 particle is provided by models where the baryon number U(1)$_B$ is gauged such as

$$\mathcal{L}_{\mathrm{U}(1)_B} = \mathcal{L}_q + \mathcal{L}_\chi - \frac{1}{4} F'_{\mu\nu} F'^{\mu\nu} + \frac{M^2_{Z'}}{2} Z'^{\mu} Z'_{\mu}\,, \tag{3.1}$$

where the actual mass generation mechanism is not relevant here. The quarks are the only SM fermions charged under this new gauge symmetry thus:

$$\mathcal{L}_q = +\frac{g_Z}{2} Z'_{\mu} \times \frac{1}{3} \sum_q \bar{q} \gamma^{\mu} q\,, \tag{3.2}$$

while for the DM particle χ

$$\mathcal{L}_\chi = \begin{cases} i\bar{\chi}\gamma_\mu \partial^\mu \chi - m_\chi \bar{\chi}\chi + \frac{g_Z}{2} Z'^{\mu} \times z_\chi \bar{\chi}\gamma_\mu \chi \\ \partial_\mu \phi^\dagger_\chi \partial^\mu \phi_\chi - m^2_\chi \phi^\dagger_\chi \phi_\chi + \frac{g_Z}{2} Z'^{\mu} \times i z_\chi \left[(\partial_\mu \phi^\dagger_\chi)\phi_\chi - \phi^\dagger_\chi \partial_\mu \phi_\chi \right] \end{cases}, \tag{3.3}$$

where the only important requirement on χ is that it is long-lived enough to reach the detector. The U(1)$_B$ is anomalous and the cancellation of anomalies could lead to additional strong constraints as discussed in [38, 39]. However, these constraints depend on whether the anomalies are canceled by fermions chiral or not under SM gauge symmetries, hence they are UV-dependent and we will not include them while comparing sensitivity of various low energy probes.

JHEP05(2019)028

$M_{Z'}$[GeV]	$N_{\rm evt}$	$\epsilon_{\rm ga}$[%]
2	$1.44 \cdot 10^{6\ +1.5\%}_{\ -1.5\%}$	14.1
3	$1.15 \cdot 10^{5\ +2.5\%}_{\ -2.5\%}$	5.47
4	$1.22 \cdot 10^{4\ +4.3\%}_{\ -3.2\%}$	3.1
5	$1.81 \cdot 10^{3\ +4.0\%}_{\ -4.1\%}$	2.0
6	$3.29 \cdot 10^{2\ +4.6\%}_{\ -5.0\%}$	1.5
7	$6.84 \cdot 10^{1\ +5.6\%}_{\ -5.7\%}$	1.1
8	$1.66 \cdot 10^{1\ +6.3\%}_{\ -5.6\%}$	0.89
9	$4.48^{\ +6.7\%}_{\ -6.9\%}$	0.76
10	$1.26^{\ +7.0\%}_{\ -7.3\%}$	0.67

Table 2. Number of DIS dark matter scattering events ($N_{\rm evt}$) as a function of the mass of the Z' mediator for the benchmark point reported in the listing in appendix D.2. $\epsilon_{\rm ga}$ is the geometrical acceptance of the detector.

The existing bounds on the Z' coupling in the 1–10 GeV mass range come from the Z' exchange induced invisible decays of quarkonia such as $\Upsilon \to \chi\bar{\chi}$ and $J/\psi \to \chi\bar{\chi}$ (see [40]). Monojet searches at hadron colliders set a bound on g_Z, the strongest one coming from a CDF search [41, 42] at Tevatron, g_Z^2 BR$(Z' \to \chi\chi) < 1.4 \times 10^{-2}$. Moreover, existing and previous neutrino facilities like MiniBooNE (as off-axis detector for the 120 GeV Main Injector beam) could have sensitivity to few GeV leptophobic Z' as discussed in [32, 43, 44] where it is shown that a reanalysis of existing data could set the strongest bounds on an ample region of the parameter space.

In this study, we exploited the prompt production mode of MadDump for the generation of dark matter particles in the s-channel for an almost on-shell Z'. We use our own version for the UFO file for this model, which is available in the MadDump directory. We scan over the mass of the Z' (that is the only relevant parameter) in the range $[2, 10]$ GeV with equal steps of 1 GeV. For each point we have generated 2 M events for the Z' production and decay and subsequently 10k dark matter nucleon DIS interactions. With this statistics the errors on the inclusive number of scattering events in the detector, estimated with the techiniques discussed in appendix B, turn out to be around 10%, as shown in table 2. In this table we also show the fraction of events which passes the detector acceptance that ranges from $\sim 14\%$ for $M_{Z'} = 2$ GeV to $\sim 0.6\%$ for $M_{Z'} = 10$ GeV. Exploiting a small workstation with sixteen cores, we have got the following timings for the complete simulation of each benchmark point:

- production: $\sim 20'$ ($15'$ in I/O operations for the combination of the partial results)
- fit: $\sim 1'$
- interaction: $\sim 4'$.

JHEP05(2019)028

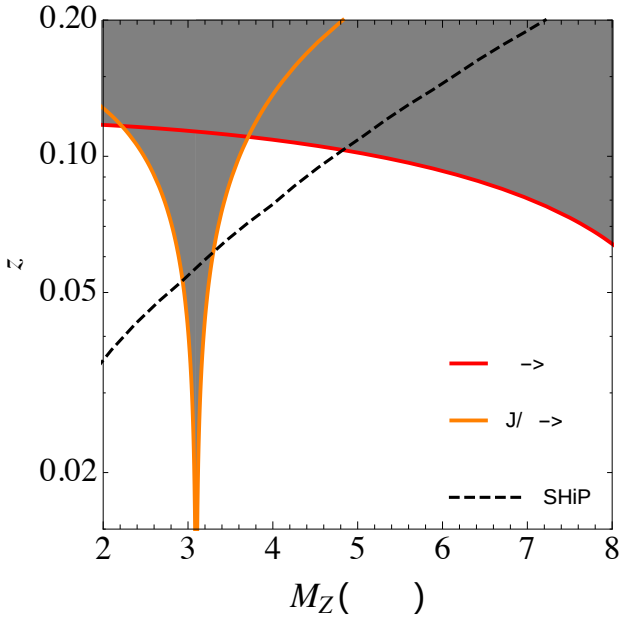

Figure 8. Sensitivity plot to a GeV leptophobic force at a SHiP like experiment obtained with MadDump assuming 9×10^5 neutrino deep inelastic background events [7]. The DM mass has been fixed to 750 MeV.

Based on [7] we assume 9×10^5 background events. In figure 8 we present the potential sensitivity of SHiP for 2×10^{20} proton on target (POT) to this scenario and we compare it with the above mentioned existing constraints. The strongest constraints come from quarkonia decays, while in this region of the parameter space the sensitivity of monojet searches is not sufficiently sensitive to probe new regions. SHiP can explore new regions of the parameter space for Z' masses below 5 GeV achieving a sensitivity comparable to the projections for MiniBooNE [32, 43, 44]. In the simulations we assumed $m_\chi = 750$ MeV, however we checked that the dependence on the DM mass is negligible. For lighter Z masses other production mechanism become relevant such as meson rare decay or proton-bremsstrahlung. A strong sensitivity has been obtained by MiniBooNE collaboration performing an analysis elastic DM-quark scattering running the experiment in beam dump mode [45]. It would be interesting for a future work to explore the sensitivity of SHiP in this region of the parameter space.

3.1.2 Leptophobic scalar and pseudo-scalar portal

Another interesting possibility to consider is a leptophobic force mediated by a scalar or pseudo-scalar particle.

We consider the following simplified model

$$\mathcal{L}_{S/a} = \frac{1}{2}\partial^\mu S \partial_\mu S - \frac{1}{2}m_S^2 S^2 + S\sum_i g_S^i \bar{q}_i q_i - S\bar{\chi}\chi + i\bar{\chi}\gamma_\mu \partial^\mu \chi - m_\chi \bar{\chi}\chi, \tag{3.4}$$

with $i = u, d, s, c, b, t$; as before, χ is a Dirac fermion stable or long-lived enough to cross the SHiP detector. In the case of a real scalar S the interaction with quarks could arise

JHEP05(2019)028

via the renormalisable interaction

$$\mathcal{L}_S \supset g_S S H^\dagger H \,, \tag{3.5}$$

which induces a singlet-Higgs mixing $\sin\theta$ such as the singlet S inherits couplings to the SM fermions:

$$g_S^i = y_i \cdot \sin\theta \,, \tag{3.6}$$

where y_i is the SM Yukawa coupling of the fermion i. A different flavor structure from the SM for the singlet-fermion coupling could be arranged via the dimension five operators, that is:

$$\mathcal{L}_S \supset \sum_i \left(\frac{\tilde{g}_S^{q_i q_i}}{\Lambda} S H_c \bar{Q}_L^i d_R^i + \text{h.c.} \right) \tag{3.7}$$

and

$$g_S^i = \frac{\tilde{g}_S^{q_i q_i} v}{\Lambda} \,, \tag{3.8}$$

where Λ is the cutoff above which either extra Higgs bosons or vector-like leptons are expected. Depending on the origin of the interaction among S and the quarks, bounds from Higgs invisible decay and/or electroweak precision measurements could be relevant. However, we will not discuss them due to their dependence on the UV-completion. Moreover, we assume that CP is a good symmetry of the Lagrangian (see for instance [46] for a discussion of possible constraints).

We consider the benchmark scenario where the scalar S couples to up and down quarks (see [46]). We rely on the general dark matter model given in ref. [47] and the corresponding UFO file for the simulation. We scan over the relevant parameter, the mass of the scalar mediator S, in the range $[2, 10]\,\text{GeV}$ with equal steps of $1\,\text{GeV}$. We have generated $100\,\text{k}$ events for the scalar mediator production and decay events and subsequently $10\,\text{k}$ dark matter nucleon DIS interactions. This statistics leads to errors around 10% for the inclusive number of scattering events in the detector, as reported in table 3. In the same table we report also the fraction of dark matter events which cross the detector surface, which ranges from $\sim 16\%$ for $m_S = 2\,\text{GeV}$ to $\sim 4\%$ for $m_S = 10\,\text{GeV}$. In this case, we get the following timings (running on the same workstation as in the previous example):

- production: $\sim 4'$
- fit: $\sim 1'$
- interaction: $\sim 4'$.

In figure 9 we show the sensitivity at SHiP considering as before DIS as signal events. In this case the only existing bounds come from the CDF monojets bounds [7, 41] and we notice that SHiP could constrain new regions of the parameter space with this proposed analysis. The analysis suggested in [32, 43, 44] for MiniBooNE could also in principle achieve a similar sensitivity, but a detailed study in this regard is still missing. As for the previous study, we fixed $m_\chi = 750\,\text{MeV}$, but the χ dependence is negligible. For lighter S mass it would be necessary to perform a new study considering different production modes such as rare meson decay (i.e. ρ) or proton-bremsstrahlung.

JHEP05(2019)028

$M_{Z'}$[GeV]	$N_{\rm evt}$	$\epsilon_{\rm ga}$[%]
2	$11.6^{+7\%}_{-2\%}$	16.3
3	$2.01^{+7\%}_{-5\%}$	8.5
4	$3.41 \cdot 10^{-1}\,^{+2\%}_{-12\%}$	6.2
5	$7.05 \cdot 10^{-2}\,^{+7\%}_{-10\%}$	5.1
6	$1.78 \cdot 10^{-2}\,^{+6\%}_{-10\%}$	4.5
7	$5.09 \cdot 10^{-3}\,^{+7\%}_{-11\%}$	4.2
8	$1.52 \cdot 10^{-3}\,^{+11\%}_{-8\%}$	3.9
9	$5.13 \cdot 10^{-4}\,^{+10\%}_{-9\%}$	3.7
10	$1.83 \cdot 10^{-4}\,^{+10\%}_{-8\%}$	3.7

Table 3. Number of DIS dark matter scattering events ($N_{\rm evt}$) as a function of the mass of the scalar mediator S for the benchmark point reported in the listing in appendix D.2. $\epsilon_{\rm ga}$ is the geometrical acceptance of the detector.

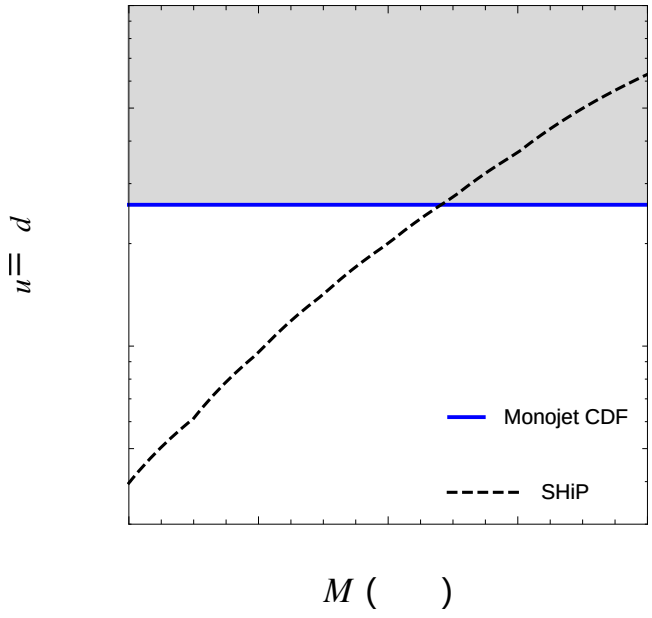

Figure 9. Sensitivity plot to a GeV scalar mediator at a SHiP like experiment obtained with MadDump assuming 9×10^5 neutrino DIS events compared to existing bounds from CDF [7, 41].The DM mass has been fixed to 750 MeV.

JHEP05(2019)028

3.2 Electron-DM scattering: the dark photon

As benchmark model to study DM-electron scattering we consider a new gauge boson associated to an abelian gauge symmetry U(1)′, A', kinetically mixed with the photon [48], namely a dark photon (DP). The relevant Lagrangian corresponds to:

$$\mathcal{L}_{A'} = -\frac{1}{4}F'_{\mu\nu}F'^{\mu\nu} + \frac{m^2_{A'}}{2}A'^{\mu}A'_{\mu} - \frac{1}{2}\epsilon\, F'_{\mu\nu}F^{\mu\nu}\,, \tag{3.9}$$

where ϵ is the DP-photon kinetic mixing. We further assume the existence of a particle χ either a scalar or a fermion charged under the new gauge symmetry U(1)′ and stable at least compared to the scale of SHiP, hence we also add the following Lagrangian:

$$\mathcal{L}_{\chi} = \begin{cases} \bar{i}\bar{\chi}\gamma_{\mu}\partial^{\mu}\chi - m_{\chi}\bar{\chi}\chi + g_D A'^{\mu} \times \bar{\chi}\gamma_{\mu}\chi, \\ \partial_{\mu}\phi^{\dagger}_{\chi}\partial^{\mu}\phi_{\chi} - m^2_{\chi}\phi^{\dagger}_{\chi}\phi_{\chi} + g_D A'^{\mu} \times i\left[(\partial_{\mu}\phi^{\dagger}_{\chi})\phi_{\chi} - \phi^{\dagger}_{\chi}\partial_{\mu}\phi_{\chi}\right]\,, \end{cases} \tag{3.10}$$

We choose as benchmark point $m_{\chi} = m_{A'}/3$ and $\alpha_D = \frac{g^2_D}{4\pi} = 0.5$ as in [49].

For this case study, we have used the decay-interaction mode of MadDump. The incoming meson fluxes has been generated with Pythia8, having care to store only the final state mesons which decayed directly in photons. This means that in a decay chain $\eta \to 3\pi_0 \to 6\gamma$ only the $3\pi_0$ are stored, while a η meson is stored in the list if it decayed directly into 2γ. With this caveat, we can limit ourselves to consider only one decay channel for each of the mesons included in our analysis:

- $\pi_0 \to 2\gamma$;
- $\eta \to 2\gamma$;
- $\omega \to \gamma\pi_0$.

We exploited the general UFO model for spin-1 as reference model for the DP [47, 50]. The meson decays has been modeled applying a standard effective field theory (EFT) approach. Indeed, for the most interesting case in which the DP is almost on shell, the decay process can be approximated by the tree-level vertex depicted in figure 10 at first order in the EFT expansion. We added the meson particles and the minimum set of new interactions required to deal with their decays directly in the UFO file, on top of the reference model. We simulated 100 k POT events, which, in terms of meson yields/POT, resulted in: ~ 6/POT for pions, ~ 0.3/POT for η's and ~ 0.07/POT for ω's. For electron scattering events, according to the SHiP technical proposal [7], we consider the following selection cuts:

- $1\,\text{GeV} \leq E_e \leq 20\,\text{GeV}$
- $10\,\text{mrad} \leq \theta_{\chi-e} \leq 20\,\text{mrad}$

where $\theta_{\chi-e}$ is the angle between the incoming DM particle and the outgoing electron. In table 4, for the case of pions decays, we compare the fraction of events passing the cuts on the recoiling electrons with our setup and increasing the statistics on the interaction

JHEP05(2019)028

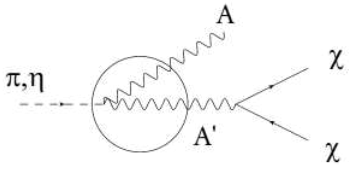

Figure 10. Effective field theory approach to production of DP from rare meson decay.

$M_{A'}$[MeV]	$\epsilon_{\text{cuts}}(10\,\text{k})$[%]	$\epsilon_{\text{cuts}}(100\,\text{k})$[%]
10	1.74	1.64
20	6.67	6.44
30	12.9	12.7
40	18.8	18.9
50	23.5	24.0
60	28.3	28.0
70	30.9	31.3
80	34.1	33.3
90	35.0	34.5
100	34.9	35.3
110	34.8	35.6
120	35.7	36.0
130	36.0	35.7

Table 4. Fraction of dark matter-electron scattering events ϵ_{cut} passing the cuts on the recoil electrons as a function of the mass of the DP A' for the benchmark point reported in the listing in appendix D.3. We compare the results obtained by incresing the statistics on the requested interaction events from 10 k to 100 k.

events to be generated. The results show that, for this analyses, the original statistics is sufficient to reach the 10% accuracy goal. We considered one meson species at time, and scanned over the relevant parameter space, for masses of the DP below the corresponding meson mass. For the case of the pions, which are the most numerous particles, the time per scan point has been $\sim 20'$ on a 4-cores CPU. The most time consuming tasks are the I/O operations related to the meson decay process, which took $\sim 14'$ of the whole time per benchmark point.

In figure 11 we present in the $(m_{A'}, \epsilon)$ plane the SHiP sensitivity compared to existing bounds, described in details in [49]. In the region of interest, the strong experimental constraints come from the monophoton BaBar search [51] and NA64 [52] via a missing energy analysis. Assuming $\alpha_D = 0.5$, experiments looking at electron-DM scattering such as MiniBooNE [53], LSND [54], and E137 [55] achieve a better sensitivity than NA64 so their reach is also presented here. An even stronger reach for $m_{A'} \lesssim 300\,\text{MeV}$ could be reached by NOνA experiment at Fermilab by recasting existing data as shown in [56]. We assume 284 electron-neutrino scattering events as background following [7]. We simulated events both for electron-ϕ_χ scattering and DIS events comparing their sensitivity in figure 11.

JHEP05(2019)028

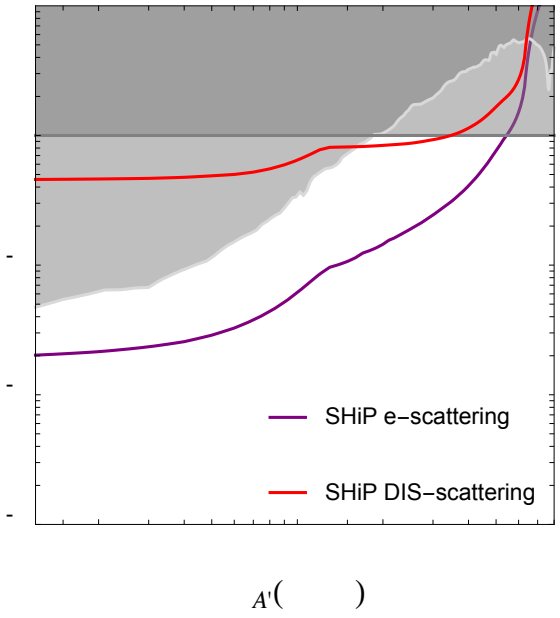

Figure 11. SHiP sensitivity for a Sub-GeV dark photon emitted by rare meson decays of π^0, η and ω obtained with MadDump. For all production modes both electron-DM scattering and DIS are considered considering respectively 284 and 9000 background events. The gray region is excluded by current probes, the strongest are BaBar mono-photon search [51] and MiniBooNE [53]. The dark gauge couplings is chosen to be $\alpha_D = 0.5$ and the ration between DP and DM mass is 3.

As expected, the electron sensitivity is significantly better than the one achievable with DIS since for $m_\chi \lesssim \Lambda_{QCD}$ the electron-DM scattering rate is comparable to the DM-quark scattering rate and it has the advantage of a reduced neutrino background. Our prediction here is conservative because we do not include potentially important contributions to the production stage like the decays from mesons produced in the cascade process and the prompt production. For sub-MeV A' masses, the SHiP sensitivity stays flat. However, such a light dark photon is disfavored by cosmology and important constraints arise from the Borexino and LSN experiments as discussed in [57]. Furthermore, in this region of the parameter space, χ could not represent the dominant DM candidate due to strong cosmological constraints as discussed in [58].

4 Conclusion

In this paper we have presented a new MG5aMC plugin called MadDump that allows for the generation of events where the production of a particle and its detection are separated by a long distance. In order to install it, it is enough to type "install maddump" within MG5aMC.[3] The main input provided by the user are the geometry of the experiment and the physics model under investigation. With these ingredients event generation corresponding to one or more benchmark scenarios can be performed automatically. We have shown illustrative examples based on different BSM scenarios and production/detection

[3]For further details, please refer to https://launchpad.net/maddump.

JHEP05(2019)028

mechanisms and computed the corresponding number of events that would be produced at the SHiP experiment. The framework is fully general and can be applied to any BSM model and experiment at a beam dump facility that aims to test it. Our tool could be employed for a number of studies, from the search of new feebly interacting particles to the study of elusive SM processes like tau neutrino cross section at present and future beam dump experiments.

Acknowledgments

We are thankful to Eduardo Cortina, Giovanni De Lellis, Antonia Di Crescenzo, Jan Hajer and Roberta Volpe for useful comments on the manuscript and to Patrick deNiverville for discussions. LB thanks Zahra Ghorbani Moghaddam for useful conversations. The work of LB and FT has been supported in part by the Italian Ministry of Education and Research MIUR, under project n^{o} 2015P5SBHT and by the INFN Iniziativa Specifica ENP. FM is supported by the European Union's Horizon 2020 research and innovation programme as part of the Marie Sklodowska-Curie Innovative Training Network MCnetITN3 (grant agreement no. 722104) and by the F.R.S.-FNRS under the 'Excellence of Science' EOS be.h project n. 30820817.

A Techniques for event generation

Consider the problem of generating unweighted points in a 2D-space according to the distribution

$$P(x, y)dxdy = f(x, y)g(x, y)dxdy\,, \tag{A.1}$$

where $g(x, y)$ is a modulation function whose expression is supposed to be known analytically. More precisely, we are mainly interested in the problem of generating unweighted y values given a fixed $x = \overline{x}$ according to the profile function

$$\phi_{\chi}(y)dy = P\left(\overline{x}, y\right) dy\,. \tag{A.2}$$

When the function $f(x, y)$ is given in closed form the problem reduces to generating points according to a given function $P(x, y)$ and it can be accomplished by standard Monte Carlo techniques, using for example the classic hit-or-miss algorithm. Here we consider the more interesting situation in which the function $f(x, y)$ is only available numerically indirectly from sample of events.

One can re-interpret it as a fitting problem. The function $f(x, y)$ is given in an approximated way, with a level of precision which can be in principle reduced at will (by generating more points) but at each step it is finite, as a 2D histogram built out of events. In its standard formulation, the task of obtaining a fit from an histogram consists basically of two different parts:

- the choice of the model, i.e. an n-parameter family of functions together with the cost function of the fit;
- minimisation of the cost function.

JHEP05(2019)028

In so doing the result is given by a function supplemented with extra information on the accuracy of the fit (covariance matrices, goodness of the fit, etc). Fitting a function, even in the "simple" 2D case, is however not always trivial. In particular, aside the technical aspects underlying the minimisation procedure, a certain amount of knowledge of the function to be fitted is required (in order to choose a reasonable class of models). For our purposes, no a priori assumptions can be formulated on the behavior of the function $f(x, y)$, as, in general, it can result from very different classes of physical processes. For this reason, we look for a procedure that allows to automatize the process.

Though an analytical fit has advantages (including also the possibility of smoothing a discrete data sample in to continuous distribution), such a level of accuracy is not strictly required in order to perform the generation of the unweighted events and we do not adopt it. Our approach is based on importance sampling and variance reduction methods implemented in Monte Carlo integrator algorithms. The strategy is based on the flattening of the integrand function via a numerical adaptation of the integration grid. Moreover, once the grids are available, they can be used to regenerate unweighted points according to the integral function.

In our implementation, we have devised a complete deterministic procedure to construct a grid, very closely the above concept of adaptive grid. In what follows, we will give a detailed description of our algorithm together with some validation examples.

A.1 Grid construction

As a first example, let us consider the case in which the modulation function $g(x, y)$ reduces to the identity map. As simple as it may appear (in this case $P(x, y)dxdy = f(x, y)dxdy$ and an unweighted generator for that distribution is assumed to be known), it allows us to clarify a few useful points. First, it may happen that generating events with the grid is more efficient (for what concern both time and space resources), or more usable in some sense, than exploiting the original generator. This is in fact the case in our applications, in which the unweighted generator has a very complex structure and the 2D events we interested in are a tiny part of the whole result. For this reason, it is not only an illustrative case, leading to a clearer illustration of the basic concepts, but it is relevant *per se*.

We assume to have at our disposal a sample of N unweighted points (x, y) distributed according to the function $f(x, y)$. Our aim is to generate unweighted events distributed according to the same distribution. Starting from the available points, the profile of the function $f(x, y)$ is given by the heights of a 2D histogram with bins of equal size. The idea is that of resizing the bins in such a way to flatten the histogram, or, equivalently, to have the same number of points lying in each bin. In this way, the distribution of the bins will follow the behavior of the function: they will be denser and smaller near the region where $f(x, y)$ is peaked and sparse and bigger where it is flat. The resulting 2D map will retain almost the full information of the 3D plot, and it is very similar to the idea of a contour plot.

In order to obtain such a parametrisation, we employ a decision-tree-like algorithm, which is very simple and efficient. Before describing it, a technical remark is needed. Adaptive grids are often constructed with lines parallel to the axis coordinates. This is

JHEP05(2019)028

efficient in all the situations where the function can be expressed in the factorised form

$$f(x, y) = f_1(x) f_2(y).$$

A great improvement is given by an approach in which irregular grids, made of cells of different sizes, are allowed, as in the case of the FOAM algorithm [34]. The cells adapt better to the behavior of the function reproducing it in a more faithful way, for example near circular peaks. The cell represents the basic object of our algorithm. A cell can be split in two cells along the x-direction (horizontally) or the y-direction (vertically). Given these basic ingredients, the algorithm proceeds as follows:

1. start from a cell containing all the available points;
2. alternate an horizontal split and a vertical split, in such a way that, in each of the two splits, half of the point fall in a subcell and half in the other one;
3. repeat step 2 for each subcell until the number of point for cell is lesser/equal than a prefixed value (*exit condition parameter*).

It is clear that the above procedure gives the grid we are looking for. The exit condition parameter $n_{\min}$ controls the grain of the mesh. The choice of its value is based on the compromise between having it small for a finer grain and having a sufficient number of points per bin to be statistical significant.

We now restore the proper role of the modulation function $g(x, y)$, which as mentioned above, can be arbitrary yet to be expressed in an analytical form. It can be viewed as a reweighting of the original sample of points:

$$(x_i, y_i, 1) \to (x_i, y_i, g(x_i, y_i)) \,,$$

where we have conventionally set to 1 the common weight of the unweighted sample. We have

$$\langle P \rangle_{\text{uniform}} = \int g(x, y) f(x, y) dx dy = \int g(\xi, \eta) d\xi d\eta = \langle g \rangle_{\text{f}}$$

where the notation $\langle \cdot \rangle_{\text{pdf}}$ denotes the average with respect to the pdf in the subscript. Under the hypothesis $f(x, y)$ is a distribution function, a well-defined change of variables is implicitly given by the relation

$$f(x, y) dx dy = d\xi d\eta$$

where the function f is the Jacobian of the transformation. Furthermore, if also g has a definite sign it is possible to perform an extra change of variables

$$\langle g \rangle_{\text{f}} = \int g(\xi, \eta) d\xi d\eta = \int ds dt = \langle 1 \rangle_{\text{fg}}.$$

This relation proves the equivalence between unweighted generation of the product distribution $f \cdot g$ and the generation reweighted by g starting from a sample of unweighted points generated according to f.

JHEP05(2019)028

We are now ready to generalise the previous case. We require that the rebinning procedure leads to a grid with (almost) the same weight w for each bin, with the definition of the weight $w(b)$ of the bin b given by

$$w(b) = \sum_{(x_i,y_i)\in b} g(x_i, y_i).$$

The generalisation of the algorithm is straightforward

1. start from a cell containing all the available points;
2. alternate an horizontal split and a vertical split, in such a way that, in each of the two splits, each subcell have half the weight;
3. repeat step 2 for each subcell until its weight is greater than the prefixed value w (*exit condition parameter*).

The exit condition parameter can be chosen of the form

$$w = \alpha \frac{w_{\text{tot}}}{N} \times n_{\text{min}}$$

where n_{min} has the same meaning as before and α is a dimensional factor which can be adjusted in the direction of refining the grain or increasing the number of points per bin.

By construction, the above procedure cannot handle distributions which vanish on some regions inside the fitted domain. This limitation is particularly severe in the case the distribution presents a falling-down tail and vanishes inside the fitted region. Indeed, even if the cells become larger and larger when approaching the tail, there is always a non null probability to generate points inside them, also in the empty regions. In this way, unphysical points are generated. In order to milder this limitation, we implemented a further refinement step after the mesh has been constructed. The peripheral cells, i.e. the cells which share a side with the frame of the fitted regions, are reshaped in a such a way to limit the cell to the actual region populated by the input points. We refer again to figure 4 in section 2 to appreciate the reliability of this improvement.

A.2 Example

As a validation example, we consider the situation in which both the function $f(x, y)$ and the modulation $g(x, y)$ are given analytically in order to show that the algorithm works correctly. Furthermore, we test its robustness considering a highly non-trivial case in which the modulation affects and distorts in a severe manner the original function. We take a simple Gaussian function, (see figure 12a):

$$f(x, y) = e^{-(x^2+y^2)}$$

with the following modulation

$$g(x, y) = 2\sqrt{x^2 + y^2}\cos^2(2y) + 1.$$

The product function is shown in the 3D plot in figure 12b.

JHEP05(2019)028

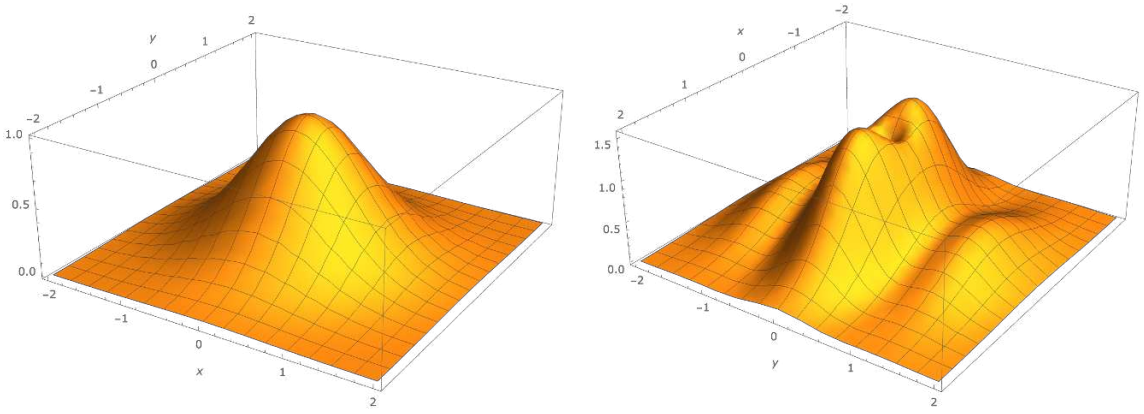

(a) Simple gaussian distribution as f function. **(b)** Full distribution after modulation is applied.

Figure 12. 3D-plot of the analytical distributions occuring in the validation example.

In figure 13a and figure 13b we report the corresponding 2D meshes obtained with our algorithm for 100 k and 1 M input points respectively. We stress that the starting point has been the generation of a sample of unweighted points distributed according to the Gaussian function. We have reweighted the points according to the modulation function and then we have applied our algorithm for weighted events. The algorithm reproduces faithfully the behaviour of the function with a level of accuracy which, as expected, improves with the number of input points.

A.3 Generation of unweighted events

Generating a 2D sample starting from the 2D mesh with the same distribution as $f(x, y)$ is trivial. By construction

- the probability of generating a point in a given cell is proportional to the inverse of its area,
- inside a cell, the probability of generating a point is uniform,

and therefore it is enough to generate an equal number of points uniformly in each cell.

Let us now turn to the issue of generating a y value according to the profile function eq. (A.2) at a given $x = \overline{x}$ point. We introduce a small resolution parameter related to the x variable ϵ such that the $x = \overline{x}$ value is fixed within the interval $[\overline{x} - \epsilon, \overline{x} + \epsilon]$. Then, the thin stripe centered in $x = \overline{x}$ with width 2ϵ and parallel to the y-axis will intercept the mesh in a subset S of cells.

We associate a normalised weight to each cell in S proportional to the ratio of the overlapping area between the stripe and the cell over the total area of the cell. Then, we pick a cell according to the value of these weights by generating a uniform random number in the interval $[0, 1]$. Finally, we generate a uniform y value within the cell. This construction solves our problem, i.e. the y values are distributed according to the profile function ϕ_χ. The procedure is independent of ϵ in the limit $\epsilon \to 0$. In practice, this means that magnitude of ϵ should be chosen as a fraction of the minimum x-width of the cells of the mesh.

JHEP05(2019)028

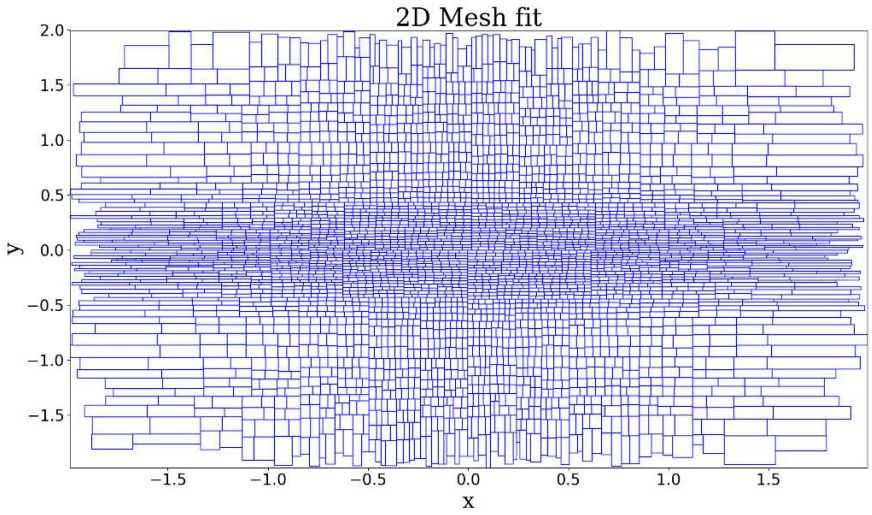

(a) 100 k input points.

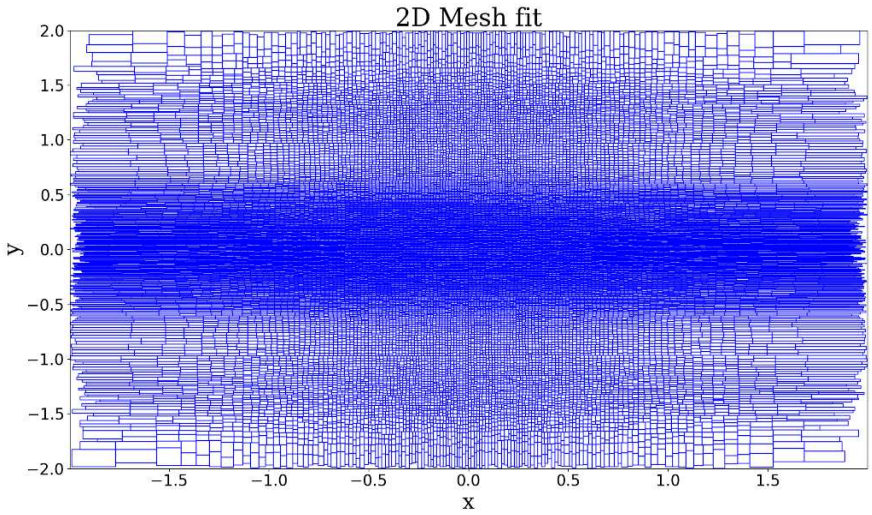

(b) 1 M input points.

Figure 13. 2D mesh obtained with our algorithm for increasing number of input points.

A.4 Example

Since an example of the generation of the entire 2D sample has been already shown in section 2, here we focus on the constrained one-dimensional generation. Let us consider again the previous example and fix a x value, for instance $\overline{x} = 0$. We generate y values distributed as the profile function (A.2) according to the above procedure. In figure 14, we plot the comparison between the generated points and the analytical profile function ϕ_χ using our meshes with 100 k points (14a) and 1 M points (14b). The generated histograms are in good agreement with the analytical curve and they reproduce well also the sharp deep in $y = 0$. The result improves by exploiting the mesh with a greater number of points giving a solid indication that the procedure is asymptotically converging to the true distribution.

JHEP05(2019)028

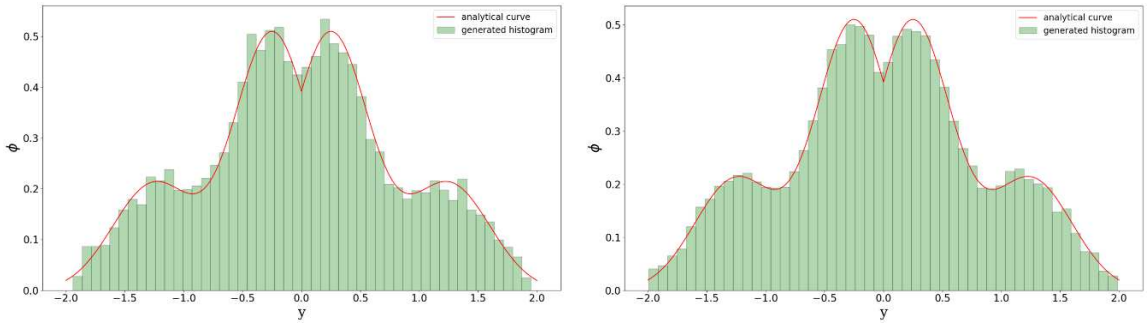

(a) Using the 100 k mesh. **(b)** Using the 1 M mesh.

Figure 14. Generation of an unweighted sample according to the 1D profile function at $\overline{x} = 0$. The distribution is normalised to 1.

B Systematic uncertainties

In summary, our fitting procedure is a way to approximate the probability density function associated to a given 2D scatter data with a piecewise function, i.e. a histogram, with an automatic choice of the bins. In the example of the previous section, we have provided a non-trivial numerical proof of concept of it. Moreover, since in that case, the analytical distribution is known a priori, we have a full control on the systematics uncertainties and the convergence of the method.

This is not the case in the practical applications, where the probability distribution is available only in the form of scatter data. As a consequence, estimating the systematics of the approximation becomes more difficult. We follow a pragmatic approach which should provide a guideline for the user to tame the systematics according to his own scopes. Despite the fact that this systematics can be made smaller and smaller by providing more and more statistics (initial input events), in practice a compromise between the accuracy goal and the actual computational resources needs to be found.

Let us start from some basic and general considerations. First, one can always separate the prediction of the total rates (including the geometrical acceptance of the detector) from those of more exclusive observables, as the angular distributions. Since the physical interaction cross section depends only on the energy, the inclusive total rates depend only on the effective dark sector particle energy distribution introduced in section 2.2.1 eq. (2.4). In our approach, we do not rely on the 2D fit to obtain this quantity. Instead, we perform a dedicated 1D fit exploiting a smoother class of functions. In this way we have a better control on the result and also on its uncertainties. Indeed, a 1D fit is a simpler operation and, since we are integrating over angles, we have access to a higher level of statistics.

The 1D fit works as follows. Starting from the input weighted data, we first build a 1D histogram and we assign to each energy bin the usual Poisson uncertainty. We then fit the histogram using a weighted cubic splines fitting. In order to assess the error on the fit, we add the possibility to vary the values within the histograms uncertainty bands. This can be done by setting the parameter `rescale_fac` in the `fit2D_card` card file, which takes values in the interval $[-1, 1]$, where 0 stands for the central value, 1 for the upper limit, -1 for the lower one. A realistic study case is given in the following subsection.

JHEP05(2019)028

We pass now to discussing the case of the 2D fit. At a fixed number of input events, the algorithm depends mainly on a unique parameters which gives the exit condition of the splitting loop. Naively, it represents the number of points which lie in each bin. Hence, there is a competition between choosing it small, to have a better description of the shape of the distribution (more bins with a smaller size), or choosing it large, to avoid to be overwhelmed by the statistical fluctuations (less bins with a larger size). The user can change this parameter by setting the value of the `npoints_cell` variable in the `fit2D_card` card file (the default value is 50). We have introduced in the code a consistency test (that can be enabled by setting to `True` the flag `fit_syst`, again in the `fit2D_card` card file) which compares the mesh obtained by varying the central value of this parameter by a factor of 1/2 and a factor of 2. To this aim, we consider the classifier

$$D(x) = \frac{P_1(x)}{P_1(x) + P_2(x)}, \tag{B.1}$$

where x represents a generic event, and $P_i, i = 1, 2$, are the probability densities we are comparing. The values of D ranges over the interval $[0, 1]$. An average value $D \sim 1$ means that $P_2(x)$ underestimates $P_1(x)$, while for $D \sim 0$ we have the opposite. For $P_1(x) = P_2(x)$, $D(x) = 1/2$. Hence, in the case the average value $D \sim 1/2$ and its standard deviation σ_D is small, we cannot distinguish between the two probability functions. The study of the D classifier put on a quantitative foot the qualitative results given by the visual inspection of the mesh grids. Its mean and standard deviation give us a measure of the global goodness of the fit. Furthermore, we can perform also a more local comparison of the angular shape at fixed value of the energy variable. We postpone a more detailed discussion to the following subsection in which we apply the above analyses to a realistic case study.

B.1 Study case: leptophobic model

As a study case, we consider the example of the leptophobic model presented in the main part of this work, given by the Lagrangian in eq. (3.1)–(3.3). Since the generation of the input DM events can be simulated directly internally in MadDump, we have a direct access to input samples of different number of events. Our setup is outlined in the script reported in the listing appendix. We select the value $M_{Z'} = 2\,\text{GeV}$ for the mass of the DM mediator. We analyse first the uncertainties on the total rates. We reported the predictions for the DM yields in table 5 for input samples of increasing statistics. The uncertainties on the predictions correspond to the 1D fit variation around the histogram error bars, as stated above. The three results are consistent within their uncertainties and, as expected, the accuracy improves increasing the statistics. We observe, that in this case, for a sample of 100 k input events, which corresponds to $100\,\text{k} \times 0.28 = 28\,\text{k}$ DM particles passing the geometrical acceptance, we already get a result accurate at the few percent level. Note that here we absorb the multiplicity factor of 2 within the definition of the geometrical acceptance ϵ.

The default value of the `npoints_cell` parameter is 50. We study what happens by varying it by a factor of 1/2 and a factor of 2. We briefly explain the strategy we followed for the comparison. We produce the three meshes corresponding to the three

JHEP05(2019)028

#evts	ϵ	#DM_evts
10 k	0.27	$25100^{+18\%}_{-15\%}$
100 k	0.282	$27700^{+4.9\%}_{-4.7\%}$
1 M	0.282	$28900^{+1.0\%}_{-1.7\%}$

Table 5. Estimates of the total DM yields for increasing numbers of input events. The uncertainties refer to the variation around the 1D fit error bars as explained in the main text. The number of input here does not include the geometrical acceptance ϵ, which is reported in the second column.

values `npoints_cell` $= 25, 50, 100$. We use the result corresponding to the central value as our reference point and we denoted by $P(x)$ the corresponding probability density. This means that we evaluate P starting from the 2D mesh as follows

$$P(x) = \frac{1}{n_{\text{cells}}} \frac{1}{A(x)} \tag{B.2}$$

where n_{cells} is the number of cells of the mesh and $A(x)$ is the area of the cells in which the point x lies. We build the two classifiers

$$D_f(x) = \frac{P(x)}{P(x) + P_f(x)}, \qquad f = l, h\,, \tag{B.3}$$

where P_l and P_h are the probabilities densities corresponding respectively to the lower and the higher values of `npoints_cell`. We generate random (uniformly distributed) points $x = (E, \theta)$ and compute the mean and standard deviation of the two classifiers. We consider the simple unbiased estimator given by the uniform average

$$\langle D \rangle_u = \frac{1}{N} \sum_{i=1}^{N} D(x_i), \qquad \sigma_u = \sqrt{\frac{1}{N-1} \sum_{i=1}^{N} [\langle D \rangle_u - D(x_i)]^2}. \tag{B.4}$$

We reported our results in the third and fifth columns of table 6, respectively for D_l and D_h. All the mean values are fairly consistent with 0.5, which is the indication that the different meshes are consistent among themselves. The standard deviation is lower for D_h, which is what is indeed expected since, with a lower `npoints_cell`, the fit is more sensitive to the statistical fluctuations of the original scatter data. Furthermore, we observe that the standard deviation decreases increasing the statistics from 10 k to 100 k events but, then, there are not any improvements from 100 k to 1 M. The explanation for this behavior is related to the vanishing tail of the distributions. Indeed, since we are fitting using piecewise functions, the accuracy of the method is worse in the long vanishing tails, where we decided to exploit a cut prescription instead of spreading uniformly the weights on a very big cell. Then, the error is dominated by the fluctuations near the boundary regions, where, however, the probability densities is approaching zero. To test quantitatively this argument, we re-weight the events accordingly to our reference probability $P(x)$, and we

JHEP05(2019)028

#evts	ϵ	$\langle D_l \rangle_u \pm \sigma_u$	$\langle D_l \rangle_w \pm \sigma_w$	$\langle D_h \rangle_u \pm \sigma_u$	$\langle D_h \rangle_w \pm \sigma_w$
10 k	0.27	0.55 ± 0.20	0.54 ± 0.03	0.48 ± 0.12	0.549 ± 0.013
100 k	0.282	0.54 ± 0.12	0.525 ± 0.015	0.50 ± 0.08	0.518 ± 0.005
1 M	0.282	0.55 ± 0.13	0.511 ± 0.005	0.47 ± 0.09	0.510 ± 0.004

Table 6. Comparison of the classifiers D_f, with $f = l, h$ calculated as weighted and unweighted averages.

consider the weighted estimators

$$\langle D \rangle_w = \sum_{i=1}^{N} D(x_i) w(x_i), \qquad \sigma_w = \sqrt{\sum_{i=1}^{N} [\langle D \rangle_w - D(x_i)]^2 w(x_i)}, \tag{B.5}$$

where the weights are given by

$$w(x) = \frac{P(x)}{\int P(x) dx}. \tag{B.6}$$

The results are reported in the fourth and sixth columns of table 6. The errors drop significantly and for the largest input sample we see that it is not possible from the practical point of view to distinguish the probability densities given by the three meshes, so that one, for instance, might choose to use the mesh corresponding to `npoints_cell`=25 since it is the finest (it has more cells with respect to the other two).

Another important aspect concerns the convergence of our method to reproduce the original data set. With this, we mean the minimum number of regenerated events $N_{\rm gen}$ needed to have a distribution which is consistent with that of the input data. Indeed, for $N_{\rm gen}$ small, we expect the regenerated distribution is dominated by the statistical fluctuations. On the other hand, we expect that after having reached the desired level of agreement, further generations of events will not spoil the convergence. The naive expectation would be to have $N_{\rm gen}^{\rm min} \gtrsim N_{\rm input}$. For a quantitative analysis, we rely again on the classifiers introduced above. In the following, we outline our strategy. We fix the mesh associated to the central value `npoints_cell`=50 as our reference for the 2D-dimensional data distribution. Starting from this mesh, we regenerate samples of events with increasing statistics. We perform a second fit on top of each regenerated sample obtaining new meshes. We assume that these meshes represents the approximate bi-dimensional distributions of the samples, according to eq. (B.2). We finally compute the two averages for each of the classifier $D_f(x)$, where now $f = N_{\rm gen}$ labels the regenerated samples. We report our result for the input sample of 100 k events. In this case, the effective number of input data events is 30 k, i.e. the events passing the geometrical acceptance cuts of the detector. The results are reported in table 7. They confirm on the quantitative ground our naive expectations $N_{\rm gen}^{\rm min} \gtrsim N_{\rm input}$, leading to the prescription $N_{\rm gen}^{\rm min} \sim 2$–$3 N_{\rm input}$.

We conclude this discussion on the fit systematics showing some lesser inclusive results at the level of differential distributions with respect to the polar angle. We adopted the following strategy. We select an energy value E. Then, we pick the cells in the 2D mesh fit in which E is included. We consider as energy resolution parameter some multiple (the

JHEP05(2019)028

N_{gen}	$\langle D \rangle_u \pm \sigma_u$	$\langle D \rangle_w \pm \sigma_w$
1 k	0.24 ± 0.24	0.27 ± 0.23
3 k	0.31 ± 0.20	0.35 ± 0.19
6 k	0.31 ± 0.16	0.34 ± 0.17
10 k	0.38 ± 0.16	0.43 ± 0.15
30 k	0.48 ± 0.10	0.50 ± 0.11
60 k	0.48 ± 0.10	0.50 ± 0.10
100 k	0.50 ± 0.07	0.51 ± 0.08
300 k	0.54 ± 0.07	0.55 ± 0.07

Table 7. Comparison of the classifiers D (calculated as weighted and unweighted averages) as function of the regenerated number of events N_{gen}.

default is 2) of the minimum energy width of the selected cells. This allows us to consider an energy bin centered in E with width given by the resolution parameter. Then, we consider the input data and the regenerated ones which lie in this bin and we compared their angular distributions given by standard 1D-histogram. Our choice of the energy bin size guarantees that the statistics is comparable for any starting E values. We have analyzed and compared the results obtained with the two input samples 100 k and 1 M. They are shown in figure 15. In both cases, we have used regenerated samples with $N_{\text{gen}} = 300\,\text{k}$. We found a good agreement both between data distributions for different statistics and between data and our fits which is of the order of ~ 25–30% for the 100 k case and $\sim 10\%$ for the 1 M one. As expected, in the region corresponding to the bulk of the events, the corresponding energy bin size are smaller. For example, in our study case, we observe that in the central energy range $40\,\text{GeV} < E < 150\,\text{GeV}$ the energy bin size is of order $\sim 1\,\text{GeV}$ for the 100 k input sample and the situation fairly improves for the 1 M one. On the contrary, for the value $E = 20\,\text{GeV}$ which lies on the tail of the distribution, we need a bigger bin size, ~ 16–$18\,\text{GeV}$.

The analyses performed in this section are encoded in MadDump and the user can reproduce the same studies for his particular situation. As a rule of thumb, to take *cum grano salis*, 500 k events entering the detector can be consider a reasonable amount of input statistics. Together with the default settings of the internal MadDump parameters and the choice of $N_{\text{gen}}^{\text{min}} \sim 2$–$3 N_{\text{input}}$ this should lead to an uncertainty of 1% for the total rates and 5–10% on the angular distributions, which is usually lesser than the other systematics of the simulation.

C A method to take into account the depth of the detector

Consider the scattering of a flux of incident particles impinging on a thick target. Let us fix the geometry of the problem and consider for instance a parallelepiped shape for the fiducial volume of the target. In general, the incident flux is neither collimated nor mono-energetic. For the sake of simplicity, we consider the flux to be originating from a point-like source placed on the target axis and mono-energetic. Consider a cartesian 3D reference

JHEP05(2019)028

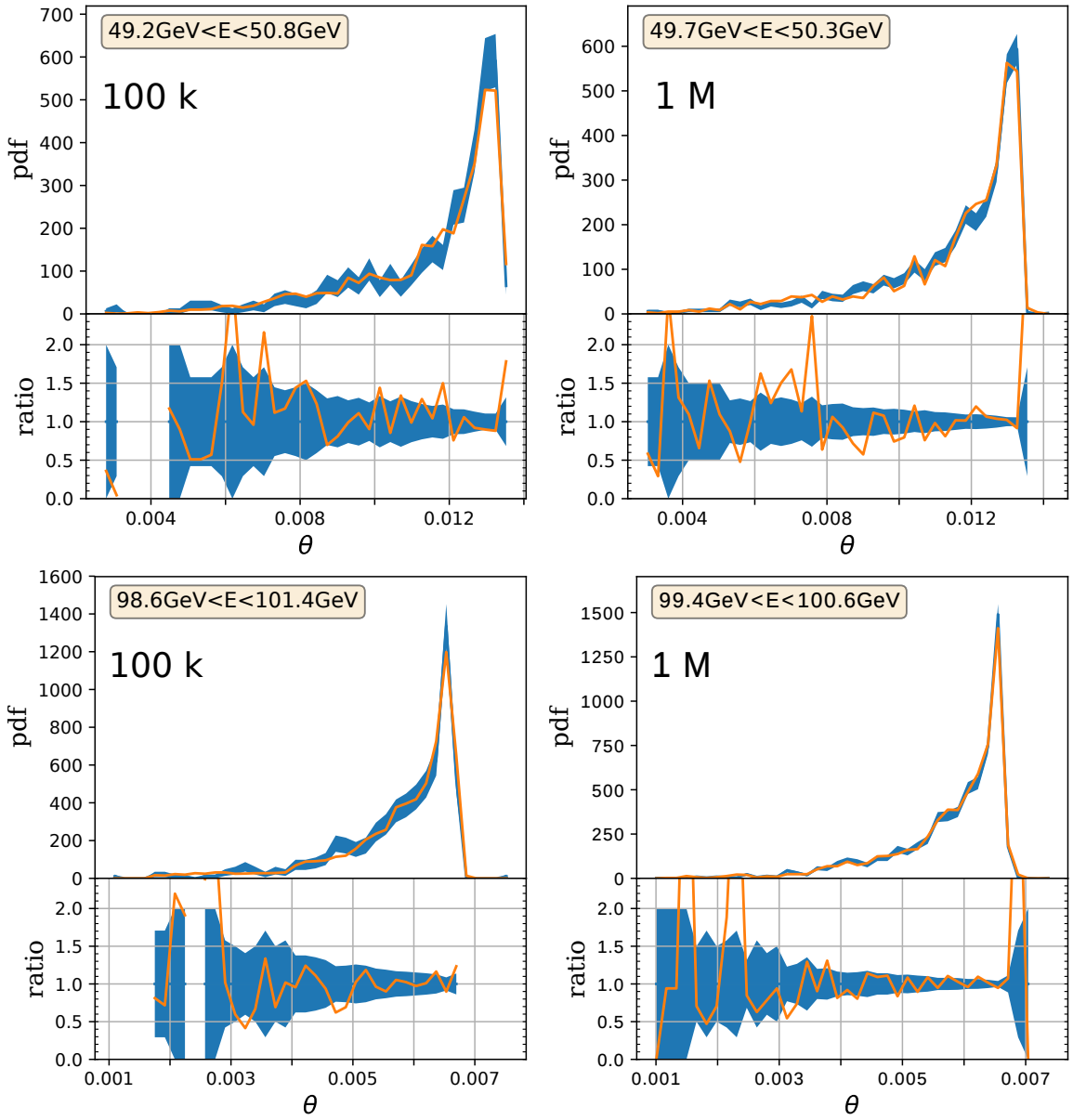

Figure 15. Normalized angular θ-distributions for different energy bins for the case of 100 k inputs events (left panels) and of 1 M inputs events (right panels). The blue band represents the original data with the associated Poissonian uncertainties. The orange line represents the histogram of the points regenerated with the 2D mesh. The energy bins size is automatically determined by MadDump in a such a way to have comparable amount of statistics in each bin.

frame in which the z-axis is along the "depth" of the target and x and y are parallel to the other dimensions. Let us subdivide the target in thin sheets along the z-axis. The number of scattered events in each sheet is given by

$$dN(z) = \int_{S(z)} dxdy \frac{\partial^2 F}{\partial x \partial y}(x, y, z)\rho(x, y, z)\sigma(z)dz\,, \tag{C.1}$$

JHEP05(2019)028

where $S(z)$ is the surface of the shell at z, F is the flux of incident particles impinging on the sheet, ρ is the number density of the target particles and σ is the interaction cross section. In the formula above, we assumed that the cross section is constant all over the surface of the sheet. Furthermore, we assume that the cross section is constant over the whole fiducial volume of the target and we consider a uniform target. Then, integrating also over the depth of the target, we get the master formula for the number of scattered events

$$N = \rho\sigma \int_{z_0}^{z_1} dz \int_{S(z)} dxdy \frac{\partial^2 F}{\partial x \partial y}(x, y, z). \tag{C.2}$$

We are interested in the situation in which the cross section is very small, i.e. we can neglect (at least in first approximation) the variation of the flux F due to the scattered particles. This means that the dependence of $\partial^2 F/\partial x \partial y$ on z is purely geometrical: from a given configuration at a point z^* it is possible to construct the flux at a new z point by prolongating the flying direction of the particles in the flux. For this reason, in the above example, even though the surface of the sheet is constant, the number of particles impinging on the different sheets along the z-axis is different:

$$\int_S dxdy \frac{\partial^2 F}{\partial x \partial y}(x, y, z) = \overline{n}(z)\,. \tag{C.3}$$

In Monte Carlo integration/generation this translates in employing different weights for the bunch of events describing the incident flux. It is still possible to use unweighted events if one considers a variant of the hit-or-miss rejection method. Here, by "unweighted events" we mean that the points have been generated according to the $dxdy\frac{\partial^2 F}{\partial x \partial y}$ distribution. Since the integrand is positive definite, enlarging the integration region we obtain the inequality

$$S(z) \geq S \implies \int_S dxdy \frac{\partial^2 F}{\partial x \partial y}(x, y, z) < \int_{S(z)} dxdy \frac{\partial^2 F}{\partial x \partial y}(x, y, z) \equiv n^*(z)\,. \tag{C.4}$$

In particular, we can choose $S(z)$ such that the above integral n^* is constant. This means that we enlarge the surface according to the radial projection starting from the point-source of the flux. Then, for the new integral, we can employ unweighted events for the flux:

$$N = \rho\sigma n^* \int_{z_0}^{z_1} dz = \rho\sigma n^*(z_1 - z_0)\,. \tag{C.5}$$

A full event is given once a z variable or equivalently a travel distance along the flying direction of the event is generated uniformly between the minimum and the maximum value inside the largest volume. Then, we accept or reject the event whether it lies or not in the true fiducial volume.

While correct, this method is not efficient as generated events can be rejected. An alternative approach entails applying a simple reweighting procedure. Intuitively, we just have to penalize the events that would be produced by particles crossing the fiducial volume of the detector over smaller paths. Indeed, a given event may contribute or not to $n(z)$ in eq. (C.3) depending whether at z it is inside or not the integration region:

$$\frac{\partial^2 F}{\partial x \partial y}(x, y, z) = \begin{cases} \frac{\partial^2 F}{\partial x \partial y}(x(z), y(z), z_0), z < d(x, y) \\ 0, z > d(x, y) \end{cases} \tag{C.6}$$

JHEP05(2019)028

where we denoted with $d(x, y)$ the z-distance after which the event goes out of the integration region. However, the weights retain a dependence on z due to the presence in the argument of the function of ($x(z)$,$y(z)$), which represent the coordinates of the particle when it crossed the sheet at z_0. If we replace x, y-coordinates by angular ones (θ, ϕ_χ) which gives the flying direction of the events, the weight will not have any residual dependence on z but the theta function $\Theta(z - d(\theta, \phi_\chi))$. This can be simply taken into account by reweighting the events as

$$\frac{\partial^2 F}{\partial x \partial y}(\theta, \phi_\chi) \times \frac{d(\theta, \phi_\chi)}{(z_1 - z_0)}\,. \tag{C.7}$$

In terms of the travel distance inside the fiducial volume of the detector $r(\theta, \phi_\chi)$, we have

$$d(\theta, \phi_\chi) = r(\theta, \phi_\chi)\cos(\theta). \tag{C.8}$$

Then, using this reweighting strategy, we can reconstruct the full event by generating uniformly the z or, equivalently, the traveled distance variable according to the actual minimum-maximum allowed by the geometry of the target.

Notice that the number of scattered events in the two cases is given by:

$$N = \begin{cases} \rho\sigma(z_1 - z_0)(n^* - n_{\text{rejected}}) \\ \rho\sigma(z_1 - z_0)\langle\overline{n}(z)\rangle, \end{cases} \tag{C.9}$$

which implies the integral condition:

$$(n^* - n_{\text{rejected}}) = \langle\overline{n}(z)\rangle. \tag{C.10}$$

D Listings

In this appendix we report the input script files used for the examples presented in the main text.

D.1 Leptophobic GeV mediator

```
import model DMZB
generate production p p > chidmsc chidmsc~
define darkmatter chidmsc
add process interaction @DIS
output leptofobic
launch
set nevents 100k
set ebeam1 400.
set ebeam2 0.938
set use_syst False
set flux_norm 19663072216.4
set prod_xsec_in_norm True
set d_target_detector 5650.0
set detector_density 3.72
set parallelepiped True
set x_side 187.0
set y_side 69.0
set depth 200.0
set testplot True
set mchidm 75
set mchidmsc 0.75
set mzb scan:[i for i in range(2,11,1)]
set wzb auto
```


JHEP05(2019)028

D.2 Scalar GeV mediator

```
import model DMsimp_UFO-full
generate production p p > xd xd~ /y1
define darkmatter xd
add process interaction @DIS /y1
output scalar
launch
set nevents 100k
set ebeam1 400.
set ebeam2 0.938
set use_syst False
set flux_norm 19663072216.4
set prod_xsec_in_norm True
set d_target_detector 5650.0
set detector_density 3.72
set parallelepiped True
set x_side 187.0
set y_side 69.0
set depth 200.0
set testplot True
set gsxr 0.0
set gsxc 0.0
set gsxd 1.0
set gpxd 0.0
set gsd11 1e-3
set gsu11 1e-3
set gsd22 0.0
set gsu22 0.0
set gsd33 0.0
set gsu33 0.0
set gpd11 0.0
set gpu11 0.0
set gpd22 0.0
set gpu22 0.0
set gpd33 0.0
set gpu33 0.0
set gsg 0.0
set gpg 0.0
set gvxc 0.0
set gvxd 0.0
set gaxd 0.0
set gpxd 0.0
set gvd11 0.0
set gvu11 0.0
set gvd22 0.0
set gvu22 0.0
set gvd33 0.0
set gvu33 0.0
set gad11 0.0
set gau11 0.0
set gad22 0.0
set gau22 0.0
set gad33 0.0
set gau33 0.0
set mxd 0.75
set my0 scan:[i for i in range(2,11,1)]
set wy1 auto
set ymdo 2.462206e+02
set ymup 2.462206e+02
```

JHEP05(2019)028

D.3 DP from pion decays

```
import model DM_mesons_2
#import the input file events ''MesonFulx.hepmc''
import_events decay ./MesonFlux.hepmc
decay pi0 > y1 a, y1 > xd xd~
define darkmatter xd
add process interaction @DIS
add process interaction @electron
output DP_electron
launch
set flux_norm 2.0e20
set prod_xsec_in_norm false
set d_target_detector 5650.0
set detector_density 3.72
set Z_average 82
set A_average 207
set parallelepiped True
set x_side 187.0
set y_side 69.0
set depth 200.0
set ncores 16
set testplot True
set gvd11 -3.333333e-4
set gvu11 6.666666e-4
set gvd22 -3.333333e-4
set gvu22 6.666666e-4
set gvd33 -3.333333e-4
set gvu33 6.666666e-4
set gvl11 -1.000000e-3
set gvl22 -1.000000e-3
set gvl33 -1.000000e-3
set my1 scan1:[0.01*i for i in range(1,14)]
set mxd scan1:[0.01/3.*i for i in range(1,14)]
set wy1 auto
```


References

[1] DONuT collaboration, *Final tau-neutrino results from the DONuT experiment*, *Phys. Rev.* **D 78** (2008) 052002 [arXiv:0711.0728] [INSPIRE].

[2] OPERA collaboration, *Final Results of the OPERA Experiment on ν_τ Appearance in the CNGS Neutrino Beam*, *Phys. Rev. Lett.* **120** (2018) 211801 [*Erratum ibid.* **121** (2018) 139901] [arXiv:1804.04912] [INSPIRE].

[3] NA62 collaboration, *Search for heavy neutral lepton production in K^+ decays*, *Phys. Lett.* **B 778** (2018) 137 [arXiv:1712.00297] [INSPIRE].

[4] M. Drewes, J. Hajer, J. Klaric and G. Lanfranchi, *NA62 sensitivity to heavy neutral leptons in the low scale seesaw model*, *JHEP* **07** (2018) 105 [arXiv:1801.04207] [INSPIRE].

[5] LBNE collaboration, *The Long-Baseline Neutrino Experiment: Exploring Fundamental Symmetries of the Universe*, in *Snowmass 2013: Workshop on Energy Frontier*, Seattle, U.S.A., June 30–July 3, 2013 (2013) [arXiv:1307.7335] [INSPIRE].

JHEP05(2019)028

[6] S. Alekhin et al., *A facility to Search for Hidden Particles at the CERN SPS: the SHiP physics case*, *Rept. Prog. Phys.* **79** (2016) 124201 [arXiv:1504.04855] [INSPIRE].

[7] SHiP collaboration, *A facility to Search for Hidden Particles (SHiP) at the CERN SPS*, arXiv:1504.04956 [INSPIRE].

[8] SHiP collaboration, *The experimental facility for the Search for Hidden Particles at the CERN SPS*, 2019 *JINST* **14** P03025 [arXiv:1810.06880] [INSPIRE].

[9] V.V. Gligorov, S. Knapen, M. Papucci and D.J. Robinson, *Searching for Long-lived Particles: A Compact Detector for Exotics at LHCb*, *Phys. Rev.* **D 97** (2018) 015023 [arXiv:1708.09395] [INSPIRE].

[10] D. Curtin and M.E. Peskin, *Analysis of Long Lived Particle Decays with the MATHUSLA Detector*, *Phys. Rev.* **D 97** (2018) 015006 [arXiv:1705.06327] [INSPIRE].

[11] J.A. Evans, *Detecting Hidden Particles with MATHUSLA*, *Phys. Rev.* **D 97** (2018) 055046 [arXiv:1708.08503] [INSPIRE].

[12] F. Kling and S. Trojanowski, *Heavy Neutral Leptons at FASER*, *Phys. Rev.* **D 97** (2018) 095016 [arXiv:1801.08947] [INSPIRE].

[13] J.L. Feng, I. Galon, F. Kling and S. Trojanowski, *Dark Higgs bosons at the ForwArd Search ExpeRiment*, *Phys. Rev.* **D 97** (2018) 055034 [arXiv:1710.09387] [INSPIRE].

[14] V.V. Gligorov, S. Knapen, B. Nachman, M. Papucci and D.J. Robinson, *Leveraging the ALICE/L3 cavern for long-lived particle searches*, *Phys. Rev.* **D 99** (2019) 015023 [arXiv:1810.03636] [INSPIRE].

[15] N.D. Christensen and C. Duhr, *FeynRules-Feynman rules made easy*, *Comput. Phys. Commun.* **180** (2009) 1614 [arXiv:0806.4194] [INSPIRE].

[16] C. Degrande, C. Duhr, B. Fuks, D. Grellscheid, O. Mattelaer and T. Reiter, *UFO — The Universal FeynRules Output*, *Comput. Phys. Commun.* **183** (2012) 1201 [arXiv:1108.2040] [INSPIRE].

[17] A. Alloul, N.D. Christensen, C. Degrande, C. Duhr and B. Fuks, *FeynRules 2.0 — A complete toolbox for tree-level phenomenology*, *Comput. Phys. Commun.* **185** (2014) 2250 [arXiv:1310.1921] [INSPIRE].

[18] J. Alwall, M. Herquet, F. Maltoni, O. Mattelaer and T. Stelzer, *MadGraph 5: Going Beyond*, *JHEP* **06** (2011) 128 [arXiv:1106.0522] [INSPIRE].

[19] J. Alwall et al., *The automated computation of tree-level and next-to-leading order differential cross sections and their matching to parton shower simulations*, *JHEP* **07** (2014) 079 [arXiv:1405.0301] [INSPIRE].

[20] P. Artoisenet, V. Lemaitre, F. Maltoni and O. Mattelaer, *Automation of the matrix element reweighting method*, *JHEP* **12** (2010) 068 [arXiv:1007.3300] [INSPIRE].

[21] P. Artoisenet, R. Frederix, O. Mattelaer and R. Rietkerk, *Automatic spin-entangled decays of heavy resonances in Monte Carlo simulations*, *JHEP* **03** (2013) 015 [arXiv:1212.3460] [INSPIRE].

[22] F. Ambrogi et al., *MadDM v.3.0: a Comprehensive Tool for Dark Matter Studies*, *Phys. Dark Univ.* **24** (2019) 100249 [arXiv:1804.00044] [INSPIRE].

[23] E. Conte, B. Fuks and G. Serret, *MadAnalysis 5, A User-Friendly Framework for Collider Phenomenology*, *Comput. Phys. Commun.* **184** (2013) 222 [arXiv:1206.1599] [INSPIRE].

JHEP05(2019)028

[24] E. Conte, B. Dumont, B. Fuks and C. Wymant, *Designing and recasting LHC analyses with MadAnalysis 5*, *Eur. Phys. J.* **C 74** (2014) 3103 [arXiv:1405.3982] [INSPIRE].

[25] B. Dumont et al., *Toward a public analysis database for LHC new physics searches using MADANALYSIS 5*, *Eur. Phys. J.* **C 75** (2015) 56 [arXiv:1407.3278] [INSPIRE].

[26] M. Backović, K. Kong and M. McCaskey, *MadDM v.1.0: Computation of Dark Matter Relic Abundance Using MadGraph5*, *Physics of the Dark Universe* **5-6** (2014) 18 [arXiv:1308.4955] [INSPIRE].

[27] M. Backović, A. Martini, O. Mattelaer, K. Kong and G. Mohlabeng, *Direct Detection of Dark Matter with MadDM v.2.0*, *Phys. Dark Univ.* **9-10** (2015) 37 [arXiv:1505.04190] [INSPIRE].

[28] T. Sjöstrand, S. Mrenna and P.Z. Skands, *PYTHIA 6.4 Physics and Manual*, *JHEP* **05** (2006) 026 [hep-ph/0603175] [INSPIRE].

[29] T. Sjöstrand et al., *An Introduction to PYTHIA 8.2*, *Comput. Phys. Commun.* **191** (2015) 159 [arXiv:1410.3012] [INSPIRE].

[30] J. Bellm et al., *HERWIG 7.0/HERWIG++ 3.0 release note*, *Eur. Phys. J.* **C 76** (2016) 196 [arXiv:1512.01178] [INSPIRE].

[31] M. Dobbs and J.B. Hansen, *The HepMC C++ Monte Carlo event record for High Energy Physics*, *Comput. Phys. Commun.* **134** (2001) 41 [INSPIRE].

[32] P. Coloma, B.A. Dobrescu, C. Frugiuele and R. Harnik, *Dark matter beams at LBNF*, *JHEP* **04** (2016) 047 [arXiv:1512.03852] [INSPIRE].

[33] G.P. Lepage, *A New Algorithm for Adaptive Multidimensional Integration*, *J. Comput. Phys.* **27** (1978) 192 [INSPIRE].

[34] S. Jadach, *Foam: A General purpose cellular Monte Carlo event generator*, *Comput. Phys. Commun.* **152** (2003) 55 [physics/0203033] [INSPIRE].

[35] J. Alwall, C. Duhr, B. Fuks, O. Mattelaer, D.G. Öztürk and C.-H. Shen, *Computing decay rates for new physics theories with FeynRules and MadGraph5_aMC@NLO*, *Comput. Phys. Commun.* **197** (2015) 312 [arXiv:1402.1178] [INSPIRE].

[36] O. Mattelaer, MG5AMC FAQ*: How to make a parameter scan*, https://answers.launchpad.net/mg5amcnlo/+faq/2735, accessed: 2019-02-28.

[37] P. deNiverville, C.-Y. Chen, M. Pospelov and A. Ritz, *Light dark matter in neutrino beams: production modelling and scattering signatures at MiniBooNE, T2K and SHiP*, *Phys. Rev.* **D 95** (2017) 035006 [arXiv:1609.01770] [INSPIRE].

[38] B.A. Dobrescu and C. Frugiuele, *Hidden GeV-scale interactions of quarks*, *Phys. Rev. Lett.* **113** (2014) 061801 [arXiv:1404.3947] [INSPIRE].

[39] J.A. Dror, R. Lasenby and M. Pospelov, *Dark forces coupled to nonconserved currents*, *Phys. Rev.* **D 96** (2017) 075036 [arXiv:1707.01503] [INSPIRE].

[40] M.L. Graesser, I.M. Shoemaker and L. Vecchi, *A Dark Force for Baryons*, arXiv:1107.2666 [INSPIRE].

[41] I.M. Shoemaker and L. Vecchi, *Unitarity and Monojet Bounds on Models for DAMA, CoGeNT and CRESST-II*, *Phys. Rev.* **D 86** (2012) 015023 [arXiv:1112.5457] [INSPIRE].

[42] CDF collaboration, *A Search for dark matter in events with one jet and missing transverse energy in $p\bar{p}$ collisions at $\sqrt{s} = 1.96$ TeV*, *Phys. Rev. Lett.* **108** (2012) 211804 [arXiv:1203.0742] [INSPIRE].

JHEP05(2019)028

[43] B.A. Dobrescu and C. Frugiuele, *GeV-Scale Dark Matter: Production at the Main Injector*, *JHEP* **02** (2015) 019 [arXiv:1410.1566] [INSPIRE].

[44] C. Frugiuele, *Probing sub-GeV dark sectors via high energy proton beams at LBNF/DUNE and MiniBooNE*, *Phys. Rev.* **D 96** (2017) 015029 [arXiv:1701.05464] [INSPIRE].

[45] MiniBooNE collaboration, *Low Mass WIMP Searches with a Neutrino Experiment: A Proposal for Further MiniBooNE Running*, arXiv:1211.2258 [INSPIRE].

[46] B. Batell, A. Freitas, A. Ismail and D. Mckeen, *Flavor-specific scalar mediators*, *Phys. Rev.* **D 98** (2018) 055026 [arXiv:1712.10022] [INSPIRE].

[47] O. Mattelaer and E. Vryonidou, *Dark matter production through loop-induced processes at the LHC: the s-channel mediator case*, *Eur. Phys. J.* **C 75** (2015) 436 [arXiv:1508.00564] [INSPIRE].

[48] B. Holdom, *Two* U(1)*'s and Epsilon Charge Shifts*, *Phys. Lett.* **166B** (1986) 196 [INSPIRE].

[49] M. Battaglieri et al., *US Cosmic Visions: New Ideas in Dark Matter 2017: Community Report*, in *U.S. Cosmic Visions: New Ideas in Dark Matter*, College Park, MD, U.S.A., March 23–25, 2017 (2017) [arXiv:1707.04591] [INSPIRE].

[50] M. Backović, M. Krämer, F. Maltoni, A. Martini, K. Mawatari and M. Pellen, *Higher-order QCD predictions for dark matter production at the LHC in simplified models with s-channel mediators*, *Eur. Phys. J.* **C 75** (2015) 482 [arXiv:1508.05327] [INSPIRE].

[51] BaBar collaboration, *Search for Invisible Decays of a Dark Photon Produced in e^+e^- Collisions at BaBar*, *Phys. Rev. Lett.* **119** (2017) 131804 [arXiv:1702.03327] [INSPIRE].

[52] NA64 collaboration, *Search for vector mediator of Dark Matter production in invisible decay mode*, *Phys. Rev.* **D 97** (2018) 072002 [arXiv:1710.00971] [INSPIRE].

[53] MiniBooNE DM collaboration, *Dark Matter Search in Nucleon, Pion and Electron Channels from a Proton Beam Dump with MiniBooNE*, *Phys. Rev.* **D 98** (2018) 112004 [arXiv:1807.06137] [INSPIRE].

[54] P. deNiverville, M. Pospelov and A. Ritz, *Observing a light dark matter beam with neutrino experiments*, *Phys. Rev.* **D 84** (2011) 075020 [arXiv:1107.4580] [INSPIRE].

[55] B. Batell, R. Essig and Z. Surujon, *Strong Constraints on Sub-GeV Dark Sectors from SLAC Beam Dump E137*, *Phys. Rev. Lett.* **113** (2014) 171802 [arXiv:1406.2698] [INSPIRE].

[56] P. deNiverville and C. Frugiuele, *Hunting sub-GeV dark matter with the NOνA near detector*, *Phys. Rev.* **D 99** (2019) 051701 [arXiv:1807.06501] [INSPIRE].

[57] M. Pospelov and Y.-D. Tsai, *Light scalars and dark photons in Borexino and LSND experiments*, *Phys. Lett.* **B 785** (2018) 288 [arXiv:1706.00424] [INSPIRE].

[58] C. Boehm, M.J. Dolan and C. McCabe, *A Lower Bound on the Mass of Cold Thermal Dark Matter from Planck*, *JCAP* **08** (2013) 041 [arXiv:1303.6270] [INSPIRE].

JHEP05(2019)028